

New insights in single-step hydrodeoxygenation of glycerol to propylene by coupling rational catalyst design with systematic analysis

M. El Doukkali ^{a,b,*}, S. Paul ^a, F. Dumeignil ^a

^a Univ. Lille, CNRS, Centrale Lille, Univ. Artois, UMR 8181, UCCS, Unité de Catalyse et Chimie du Solide, F-59000 Lille, France

^b University of Sultan Moulay Slimane, Multidisciplinary Faculty of Beni-Mellal, Department of Chemistry, Av. Mghila, BP 592, 23000 Beni-Mellal, Morocco

ARTICLE INFO

Keywords:

Rational catalyst design
 $\text{Mo}^{\delta+}$ active-sites
 in-situ/ex-situ analyses
 Single-step hydrodeoxygenation
 Glycerol-to-propylene routes

ABSTRACT

Glycerol-to-propylene routes involve overlapped hydrodeoxygenation (HDO) events on the active sites of heterogeneous catalysts which stability in aqueous media is a challenge. Herein, we proposed a rationalized approach to develop such catalysts by using hydrophobic-inert silica supports to protect highly reactive sub-2 nm Mo particles against leaching and sintering. Propylene yield from 84.1 % to 65.6 % were obtained on MoO_x nanoparticles at space-velocity $\sim 1.7 \text{ h}^{-1}$ and H_2 -pressure ~ 50 bar. Carburizing MoO_x nanoparticles to $\beta\text{-Mo}_2\text{C}$ leads to an extremely efficient HDO catalyst, featuring, unprecedented TOF_{propylene} ranging from $\sim 153.1 \text{ h}^{-1}$ to 226.4 h^{-1} , while $\eta\text{-MoC}$ phase gave better hydrogenation activity. Coupling in-situ XPS and kinetic data reveal that Mo^{5+} , Mo^{3+} and $\text{Mo}^{2+}\text{-C}$ species play a critical role in the HDO events. Glycerol-to-propylene progresses over MoO_x via successive $\text{Mo}^{5+}/\text{Mo}^{6+}$ and $\text{Mo}^{3+}/\text{Mo}^{4+}$ cycles, while over $\beta\text{-Mo}_2\text{C}/\eta\text{-MoC}$, it occurs mostly on carbide-oxy-carbide surface. Surface accumulation of $\text{C}_x\text{H}_y\text{O}_z$ species caused $\text{Mo}^{\delta+}$ re-oxidation, which hinders the HDO events.

1. Introduction

The development of sustainable technologies for transforming biomass into useful chemicals with improved energetic and environmental qualities, in substitution to the fossil-based ones, has been the driving force of many recent researches in heterogeneous catalysis [1,2]. Many surface-catalyzed reactions such as dehydration, dehydrogenation [3], hydrogenation [4], hydro-deoxygenation (HDO)[5] or including C-C/C-H breaking [6], have been explored in attempts to approximate the properties of the target biobased compounds to those conventionally obtained from petrol-based resources. Catalytic HDO reaction, which involves overlapped deoxygenation-hydrogenation events per-site, is a well-suited strategy as it aims simultaneously at increasing the H/C ratio of the target biomolecules. In addition, oxygen removal by C-O cleavage is thermodynamically favored under typical HDO conditions (temperature $\leq 400^\circ\text{C}$ and H_2 -pressure ≤ 100 bar) [7,8], which allow avoiding biomass degradation to coke, CO and CO_2 actually prominent at higher temperatures ($> 450^\circ\text{C}$) [9]. Therefore, such moderate conditions with less-energy consumption benefit also the techno-economic feasibility and environmental impact of the target HDO process [1,2]. However, it is yet particularly challenging to develop efficient HDO catalysts able to

work in H_2O -rich hydrothermal reaction medium for producing acceptable yield of the desired products without excessive H_2 consumption. This requires new design paradigm that can be built based on mechanistic and kinetic explorations of pertinent HDO model reactions to understand better how the oxygen can be removed with simultaneous hydrogenation in multi-oxygenated molecule without breaking the length of their carbon chain.

The HDO of glycerol that involves three -OH groups seems to be an ideal model reaction for such studies, which is encouraged by the great potential of crude bioglycerol upgrading to promote the economic competitiveness of biodiesel industry [10]. It offers stimulating opportunities to obtain value-added compounds such as ethanol [11], 1-propanol [12], glycidol [13], allyl-alcohol [14,15], acrolein [16], hydrogen [17,18], C_3 -diols [19,20], lights olefins [21,22] etc. For example, converting glycerol-to-propylene (GTP) can contribute to balance the demand/supply ratio of propylene whose market is frequently suffering from shortage [23]. Also, obtaining a massively used product through this eco-friendly GTP route (with practically null carbon footprint) will undoubtedly mitigate not only the arising environmental issues, but also those related with the mismanagement of crude glycerol. Currently, GTP route is being investigated either via high-temperature processes [9,24],

* Corresponding author at: Univ. Lille, CNRS, Centrale Lille, Univ. Artois, UMR 8181, UCCS, Unité de Catalyse et Chimie du Solide, F-59000 Lille, France.
 E-mail address: m.eldoukkali@usms.ma (M. El Doukkali).



multi-steps reactions; including triple staged reactors (ZSM-5, Pd/Al₂O₃ and H-BEA catalysts) [25], separate double-reactors (Ir/ZrO₂ and ZSM-5) [26], Tandem-processes (Pt/ ZSM-5 coupled ZSM-5) [27], dual-bed catalysts (Cu-WO_x/Al₂O₃ coupled with silica-alumina)[28] or (MoNi₂P/Al₂O₃ coupled with ZSM5) [29]. Nevertheless, the viability of these strategies is questionable[30] because they involve: *i*) Intensive energy consumption for high-temperature reactions, *ii*) extensive H₂ consumption particularly when noble metals are used, *iii*) complex catalysts combination with undefined active-sites, of which the catalytic stability is a major challenge, making difficult their pre-activation and post-use regeneration. Furthermore, the use of such catalysts mixtures is challenging under H₂ co-feeding because, as shown in **Scheme 1**, they can, instead of completely remove oxygen from glycerol to selectively form propylene, only contribute to partial C-O scission to form C₃-oxy-genates, breaks C-C and C-H bounds to produce syngas (CO_x + H₂) and compounds with shorter carbon chain length, or at the limit, saturate the C=C bound of propylene to yield propane.

To the best of our knowledge, there are only three recent works on single-step GTP reaction in the gas[22] and mixed gas-liquid[21], [31] phases. The latter shed interesting early insights using reduced MoFe elements supported on Activated Carbon (AC) that allowed reaching high propylene selectivity (~76.1 %) at nearly full glycerol conversion. These incipient studies, however, only reported initial single-step GTP activities using large-residence times of highly diluted glycerol aqueous solutions (2 wt%) in batch-reactor loaded with a high mass of catalyst (1.5 g). In addition, these catalysts were tested without adopting an approach that allows understanding the factors affecting the stability of partially reduced Mo⁵⁺ sites; hypothesized as active-sites for GTP reaction [21]. Other researchers report only Mo⁴⁺ states as preferred catalytic site for propylene formation [22], which leaves some controversy. In addition, operating in batch-reactor generated diffusion restrictions, particularly, when high loading of catalyst was used [21]. Further, it did not provide solutions for the problematic sintering and leaching of Mo and Fe metals revealed in these works [15]. This panoramic review reflects many gaps to progress towards the development of efficient enough HDO catalysts for single-step GTP route.

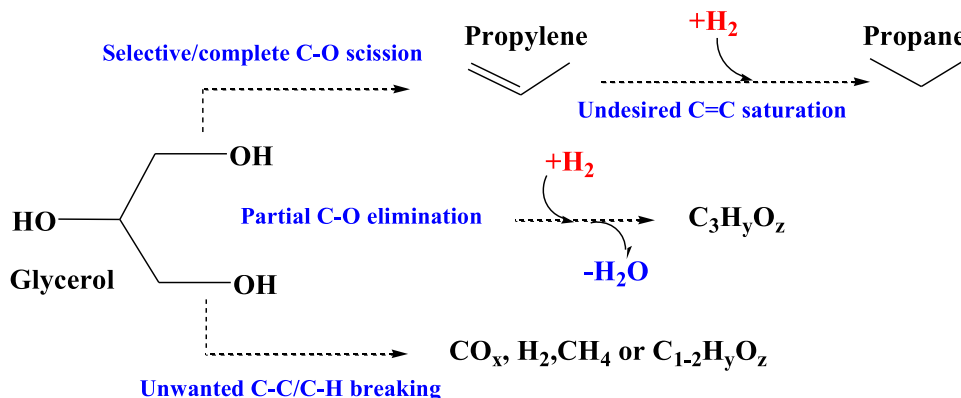
Mo oxides and carbides can be particularly relevant for C-O scission and C-C hydrogenation because of their multi-oxidation states and noble metal-like catalytic functions, respectively [21,31–33]. They have been used as impregnated or bulk phases for GTP routes[21,22,31,34], but suffered from leaching, sintering and low surface per volume ratio, particularly, when high metals content is used [21,22,31,35]. Thus, the utilization of Mo element lacks of effective experimental protocols that allows stabilizing high population of Mo species with intrinsic HDO reactivity and stability in hydrothermal medium that usually induce aging tendencies.[36].

As for the design scheme, a limited number of approaches have been explored in HDO catalysis of glycerol that encompasses randomized trials of solid catalysts [22,24,37], building steps based on *ab initio* and

DFT calculations [33,38,39], or purely *ex-situ* analyses [21,29,31]. The first approach is based on an indiscriminate screening of a large number of materials. The time and cost invested in this approach may limit their utilization even when high-throughput experimentations are used. The strategies based on numerical modelling, which aim at predicting the ideal architectural schemes for experimental catalysts design, are revolutionizing the studies of catalyzed reactions [38,40]. Even though the growing progresses of artificial intelligence and the use of machine learning can vastly reduce the calculations time, it is still unfeasible to obtain every single detail for each reaction intermediate over each site. Furthermore, the conceptual prediction is mainly evaluated based on linear scaling from ideal single-site to real catalyst with complex physicochemistry [41], causing in many times that the predictions does not fit well the real behavior under reaction conditions. The adjustment of the catalyst's properties based on *ex-situ* characterization is the most reported approach in the literature. It consists of finding correlations between the physicochemical properties of as-synthesized or post-functionalized samples and/or of the used ones, and their performance in the reaction. This relatively logical principle and easy experimental exploration allow great progresses in catalysis [42,43]; however, excessive *ex-situ* characterization of catalysts introduces uncontrolled changes in their characteristics, what upset accurate interpretations.

In an attempt to overcome the aforementioned hurdles, our research aims at combining a rationalized synthesis-functionalization tasks of Mo oxides and carbides-based catalysts, which will involve *in-situ* and *ex-situ* manipulations of sub-2 nm Mo particles and systematic mechanistic-kinetic tests to reach relevant progresses in single-step catalytic GTP route. The idea is not to only develop and compare efficient HDO catalysts that are better than those of the state-of-the art reports, but also to project a series of well-justified research actions that will be meticulously articulated within a novel and powerful approach to reach further improvements in single-step GTP route. The proposed approach enables qualitative and quantitative modulation of Mo properties, which offers therefore a potential versatility to serve as bases for building new design schemes destined to HDO of complex biobased molecules.

In this way, we will take advantage of early insights in partial reduction of Mo⁶⁺ to Mo^{δ+} intermediates, which are suggested to be critical for C-O bounds cleavage[21,31,42,44], to expand on how the population of these Mo species onto silicas supports can be intensified without penalizing their diffusion ability. So, three types of Ordered Mesoporous Silicas (OMS) were first prepared using hydrothermal synthesis, in which the loading of sub-2 nm Mo particles as controlled by melt-infiltration backed by *in-situ* DSC, X-ray scattering, and HRTEM-STEM/EDX mapping. Two requirements reinforce this synthesis combination: the hydrothermal method enables tailoring the OMS channels as desired [14], while melt-infiltration allows the liquid droplets of transition metals precursor to diffuse before its decomposition [45], allowing a direct immobilization of thin Mo nanoparticles. This in-pores



Scheme 1. Main transformation tendencies of glycerol under H₂ co-feeding.

hosting strategy can protect Mo nanoparticles against leaching and agglomeration phenomena [14]. OMS are chosen as supports due to their inert surface for C-C breaking[46] and relatively hydrophobic character expecting to provide more water-tolerant ability [46].

Determining the limit of maximal Mo loading will allow keeping the integrity of the 3D structure of OMS and their pores accessibility, and thereby, preserving their capacity to let the reactant and products diffuse properly in their porous network. In addition, it will avoid an excess of Mo loading that can remain on the outer surface of OMS, which can be subjected to sintering or leaching by hot water. Subsequent reduction or reductive-carburization, which will lean on literature to find the pertinent treatment conditions [35,47] are expected to stabilize new $\text{Mo}^{\delta+}$ -C bounds at partially reduced state ($\delta^+ < +6$). Thus, three Mo phases; MoO_x , $\beta\text{-Mo}_2\text{C}$ and $\eta\text{-MoC}$, will be further studied in bulk and dispersed forms. Parallelly, extensive kinetic tests in single-step HDO of glycerol/water mixture were carried out at different temperatures, H_2 -pressures and weight-hourly-space-velocity (WHSV) to evaluate the performance of the studied systems in C-O removing, C-C hydrogenation and/or C-C breaking. All these actions allow determining the main factors affecting the single-step GTP reaction under gas and liquid-phase conditions. Thus, considering all the mentioned issues, we discuss herein the utility of the adopted research approach to go beyond the merely progress on the single-step GTP route to exhibit a versatile re-design paradigm of HDO catalysts able to be used for a wide range of HDO reactions of other industry-relevant biobased molecules.

2. Experimental procedures

All the used reagents, of research-lab grade purity, are listed in Table S1.

2.1. Catalyst preparation

First, three type of OMS materials; SBA-15, MCM-41 and KIT-6, were prepared by modifying the procedures reported by Zhao,[48] Kresge, [49] and Kleitz,[50] respectively. Table 1 summarizes the main synthesis conditions that were chosen on purpose from existing literature [48],[49],[50] in order to obtain silica materials with the target 3D structure and meso-porosity.

In a typical synthesis, the desired structure-directing agent (P_{123} , CATB and/or BuOH , whose description is included in table S1) was mixed with deionized water, where pH of medium was adjusted by adding HCl or NH_4OH agent under stirring (500 rpm) at 38 °C or 25 °C, depending on the case, up to a complete dissolution. Then, the desired quantity of tetraethylorthosilicate (TEOS) source was added dropwise to the solution which was maintained under the same conditions during the ripening time chosen for each synthesis. The resulting hydrolysis mixture was then transferred into a closed Teflon-lined autoclave and put in an oven at the aging temperature and time set for each synthesis. Afterwards, the solid were recovered by filtration and washed with deionized water until obtaining a filtrate with neutral pH. Finally, the

Table 1

Molar composition of the starting reactants mixtures and, operating conditions of the hydrothermal synthesis.

| Material | Molar composition of starting mixture | pH | Ripening temperature (°C)/time (h) | Aging temperature (°C)/time (h) |
|----------|--|----|------------------------------------|---------------------------------|
| SBA-15 | 1 SiO_2 /0.017 P_{123} /1.1 HCl/97.51 H_2O | 2 | 38/24 | 105/72 |
| MCM-41 | 1 SiO_2 /0.13 CTAB/ 13.61 NH_4OH / 176.63 H_2O | 11 | 25/5 | 85/48 |
| KIT-6 | 1 SiO_2 /0.017 P_{123} / 1.92 HCl/1.32 n- BuOH /194.45 H_2O | 2 | 38/24 | 95/24 |

solid was dried under static air at 95 °C for one night, and about 100 mg of each as-prepared OMS were calcined under static air at 500 °C (2 °C/min) for 3 h to determine the yield of SiO_2 expected to obtain from each OMS's synthesis.

Secondly, the Mo-based OMS catalysts were prepared by dry melt-infiltration without submitting the as-prepared OMS samples to template removal. This strategy has been recently reported by our group lab [45] as an efficient route to improve the diffusion of transition metals inside porous materials. Thus, an increasing amount of $\text{H}_3\text{P}(\text{Mo}_3\text{O}_{10})_4$, 12 H_2O salt, used as the Mo precursor, was added to uncalcined SBA-15 (chosen as support model) to occupy between 3% and 93% of its total pore volume at calcined state. This loading was calculated by considering the apparent density of $\text{H}_3\text{P}(\text{Mo}_3\text{O}_{10})_4$, 12 H_2O salt (1.62 g/cm³) and the yield of SiO_2 (previously determined by calcination of SBA-15). After this, the quantity of Mo to be incorporated in MCM-41 and KIT-6 supports was estimated based on the one determined as optimal for MoO_x @SBA-15 catalyst (see Section 3.1 for further preparation details). Then, the target amount of Mo salt was manually mixed with the corresponding mass of each OMS (SBA-15, MCM-41 or KIT-6) by active grinding for 30 min to obtain a homogeneous yellow-beige powder. Then, each mixture (Mo salt + OMS support) was melt-infiltrated at 85 °C using closed-vessels to avoid the salt dehydration because this latter can strongly inhibit the diffusion of Mo salt. Finally, in attempt to check the most convenient thermal treatment for decomposing the salt and template of the melt-infiltrated Mo@OMS systems, the as melt-infiltrated Mo@SBA-15 (chosen as model) was divided in two equal portions; i) one to be calcined under static air at 500 °C (2 °C/min) for 3 h, and ii) second to be thermally reduced under a dynamic flow of 14.5 mL (STP)·min⁻¹·g⁻¹ of pure H_2 at 500 °C (2 °C/min) for 3 h. Thus, the name of pre-calcined samples was termed by C (i.e. MoO_x @SBA-15 C), while that of pre-reduced was termed by R (i.e. MoO_x @SBA-15R).

For comparison purposes, MoFe-impregnated activated carbon (AC) was chosen as reference catalyst from Zacharopoulou's[21,31] and Mota's[22] works. It was prepared following the same procedures as reported by the authors. The corresponding Mo and Fe loadings were also maintained at the same reported values; 19.3 wt% and 2.8 wt%, respectively, estimated based on the fully reduced state of metals (Mo^0 and Fe^0).

Finally, Bulk MoO_x and Fe/MoO_x were also prepared to highlight the role of the individual and combined metals because Fe species considered as stabilizing element for Mo species [34]. For this, about 16 g of $\text{H}_3\text{P}(\text{Mo}_3\text{O}_{10})_4$, 12 H_2O salt were finely dispersed in a minimal quantity of ethanol and then dried at 95 °C up to a complete ethanol evaporation. Finally, it was calcined under static air at 500 °C (2 °C/min) for 3 h to yield MoO_x . Then, about 1.02 g of $\text{Fe}(\text{NO}_3)_3$, 9 H_2O was dissolved in 5 mL of deionized water and impregnated on 1.45 g of the prepared MoO_x at 25 °C for 24 h. The Mo/Fe molar ratio was set at 4, which is identical to that of the MoFe/AC sample [21,22,31]. After water evaporation, the solid was dried at 95 °C for one night and calcined under static air at 500 °C (2 °C/min) for 3 h.

2.2. Catalyst carburization

The carburization conditions (T, H_2 flow, carburizing agent, etc.) applied before each tests were chosen from relevant literature [35,47]. Thus, chosen mass of Mo-based catalyst; previously sieved at 100–200 μm and dried overnight at 95 °C under static air, was mixed with SiC (1/3 wt. ratio) to avoid hot-spots and, then, carburized in the reactors according to the following protocols: .

1. Non-topotactic route to form $\beta\text{-Mo}_2\text{C}$, which was performed by heating under 180 mL (STP)·min⁻¹·g⁻¹ of CH_4/H_2 (18/82 vol%) up to 350 °C (5 °C/min) and then up to 700 °C (1 °C/min). The sample was held at this temperature 1 h to remove possible coke, and then cooled down under the H_2 flow alone.

2. Topotactic route to form η -MoC, which was performed by heating under 180 mL(STP).min⁻¹.g⁻¹ of C₃H₈/H₂ (10/90 vol%) up to 350 °C (5 °C/min) with a plateau for 7 h in order to facilitate the atomic exchange between oxygen and carbon at low temperature. Subsequently, the sample was heated up to 590 °C (1 °C/min) where the subsequent held and cooling were maintained the same as for Non-topotactic route.

Finally, the samples destined to further *ex-situ* characterization were softly passivated using 300 mL(STP).min⁻¹.g⁻¹ of O₂/He (1/99 vol%) for 2 h in order to avoid aggressive bulk re-oxidation. Immediate XRD analyses confirmed the formation of the target phases.

2.3. Characterization procedures

The physicochemical properties of the catalysts (i.e., composition, texture, redox/acid sites, particles location and distribution, chemical states, etc.) were further studied by a set of complementary techniques. The analytical procedures, which leans on previous works [17,47, 50–55] were described in supplementary information.

2.4. Testing conditions and performance evaluation

All catalysts were tested in the single-step HDO of glycerol using a high-throughput micro-activity setup (Flowrence®, Avantium) of the REALCAT platform [56]. This compact system integrates 4 reaction-blocks each one containing 4 continuous-flow reactors. About 65 mg of each catalyst (sieved between 100 and 200 µm) was placed between two wool plugs of SiC. Prior to test, the carburized catalysts were previously prepared according to the treatment confirmed by XRD analyses (Section 2.2), while the free-carburized samples were in-situ activated under 180 mL(STP).min⁻¹.g⁻¹ of pure H₂ up to 350 °C (5 °C/min) followed by immediate increasing of temperature up to 500 °C (2 °C/min) and held for 3 h. Then, the systems were cooled under H₂ down to the reaction temperature (318 °C or 264 °C), and the back-pressure regulator was set at the desired value (50 bar or 30 bar) by passing 693–1386 mL(STP).min⁻¹g⁻¹ of pure H₂. Once the system reached its stability, 0.26–0.36 mL(STP).min⁻¹g⁻¹ of liquid C₃H₈O₃/H₂O mixture (10/90 wt%) was introduced using a HPLC pump to reach a WHSV of 1.7 h⁻¹, 2.35 h⁻¹ or 4.7 h⁻¹. The molar ratio H₂/C₃H₈O₃ was set at 78 or 98. Time-on-stream (TOS) between 4.9 h and 14.5 h were studied. The gas and liquid products were separated at 10 °C using vapor-liquid condenser through which 35–70 mL(STP).min⁻¹g⁻¹ of He were injected as internal standard for estimating the gas-flow composition. The exhausted gases were sampled every 145 min using an online GC (Agilent 7890). The instrument is equipped with four columns: Haysep Q as pre-column, Mol-sieve 5 A for H₂ and CO separation, Poraplot-Q for CO₂, C₁-C₃ alkanes and C₂-C₃ alkenes separation, and Stabilwax for the volatile C₁-C₃ oxygenated hydrocarbons (OHCs) separation. To assess the carbon balance (CB), the condensed phase containing heavy OHCs and non-converted glycerol were also analyzed every 145 min by another offline GC-FID-2010 Plus (Shimadzu) equipped with the same Stabilwax column. The performance of catalyst was evaluated in terms of:

1. Total glycerol conversion (TGC_{gly.}) and carbon yield of each product i, (Y_i) calculated according to Eqs. 1 and 2, respectively:

$$\text{TGC}_{\text{gly.}}(\%) = \frac{\text{F}_{\text{gly.}}^{\text{Inlet}}(\text{mol}/\text{min}) - \text{F}_{\text{gly.}}^{\text{Outlet}}(\text{mol}/\text{min})}{\text{F}_{\text{gly.}}^{\text{Inlet}}(\text{mol}/\text{min})} \times 100 \quad (1)$$

$$Y_{-i}(\%) = \frac{\gamma_{i,C} \cdot \text{F}_{(i)}^{\text{Outlet}}(\text{mol}/\text{min})}{3 \cdot \text{F}_{\text{gly.}}^{\text{Inlet}}(\text{mol}/\text{min})} \times 100 \quad (2)$$

where F_{gly.}^{Inlet}(mol/min), F_{gly.}^{Outlet}(mol/min) are the molar glycerol flow-rate at inlet/outlet of the reactor, respectively, while $\gamma_{i,C}$ is the number of carbon atoms in the product (i) and F_(i)^{Outlet}(mol/min) represents its molar flow-rate at outlet of the reactor.

2. Turnover Over Frequency of glycerol-to-product i (TOF_i(h⁻¹)) that stands the rate ($-r_i$) per CO-site:

$$\text{TOF}_i(\text{h}^{-1}) = \frac{-r_i}{n_{\text{CO}}(\text{mmol.g}_{\text{Mo}}^{-1})} \quad (3)$$

In which $-r_i(\text{mmol.h}^{-1}.g_{\text{Mo}}^{-1})$ is the glycerol moles injected during an interval of time dt(h) multiplied by the yield of product i formed during this time per the mass of Mo in the test catalyst, m_{Mo}(g):

$$-r_i = \frac{dN_{\text{Glycerol}}^{\text{Inlet}}(\text{mmol})}{dt(\text{h}) \cdot m_{\text{Mo}}(\text{g})} \times \frac{Y_{-i}(\%)}{100} \quad (4)$$

Additionally, the performance of catalysts, in term of deoxygenation, hydrogenation and reforming activities, was also evaluated as:

3. Glycerol conversion by C-O scission, noted as GC_{C-O} and calculated as in Eq. 5, which reflects the C-O bonds broken in glycerol:

$$\text{GC}_{\text{C}-\text{O}}(\%) = \frac{\sum_i^n (\gamma_{i,C} - \gamma_{i,O}) \cdot \text{F}_{(i)}^{\text{Outlet}}(\text{mol}/\text{min})}{3 \cdot (\text{F}_{\text{gly.}}^{\text{Inlet}}(\text{mol}/\text{min}))} \times 100 \quad (5)$$

where $\gamma_{i,O}$ stands the number of oxygen atoms in product (i), as in the case of carbon. GC_{C-O}(%) can reach a maximum of 100% when all C-O bonds in glycerol were broken to form only alkenes and/or alkanes.

4. Glycerol conversion by C-C hydrogenation, noted as GC_{C-C} and calculated as in Eq. 6, which was estimated based on the H atoms observed in the products and the hydrogenation events required to fully convert glycerol in propane:

$$\text{GC}_{\text{C}-\text{C}}(\%) = \frac{\sum_i^n (\gamma_{i,H} - \frac{2}{3}\gamma_{i,C}) \cdot \text{F}_{(i)}^{\text{Outlet}}(\text{mol}/\text{min})}{6 \cdot (\text{F}_{\text{gly.}}^{\text{Inlet}}(\text{mol}/\text{min}))} \times 100 \quad (6)$$

where $\gamma_{i,H}$ is the number of H atoms in product (i). GC_{C-C}(%) can reach a maximum of 166.6% when all glycerol was converted into CH₄. A value of 100% indicates that all glycerol is converted into C₃H₈.

5. Glycerol conversion by C-C breaking, noted as GC_{C-/C} and calculated as in Eq. 7, which reflects the C-C bands broken in gas and liquid products:

$$\text{GC}_{\text{C}-/\text{C}}(\%) = \frac{\sum_i^n (1 - \frac{\gamma_{i,C}}{3}) \cdot \text{F}_{(i)}^{\text{Outlet}}(\text{mol}/\text{min})}{2 \cdot (\text{F}_{\text{gly.}}^{\text{Inlet}}(\text{mol}/\text{min}))} \times 100 \quad (7)$$

GC_{C-/C}(%) can reach a max value of 100% when all C-C bonds were broken to only C₁ compounds.

Moreover, the stability of catalyst in term of the loss of each activity-type was also evaluated, as in Eq. 8:

$$-\ln(C_j) = K_j \cdot t \quad (8)$$

where K_j is the pseudo-first order deactivation constant, and $C_j = \frac{C_t}{C_0}$ is the advances of a conversion type(C_t) at time t regarding the initial value of the same conversion (C₀) calculated at the first recorded data by GC (considered as t₀ time). j denotes the type of conversion activity (total conversion, C-O scission, C-C hydrogenation or C – C breaking). The K_j value was every time calculated at R² coefficient superior to 0.83.

1. The carbon balance (CB) was calculated as in Eq. 9:

$$\text{CB}(\%) = \frac{\sum_i^n \gamma_{i,C} \cdot F_{(i)}^{\text{Outlet}} (\text{mol}/\text{min})}{3 \cdot (F_{\text{gly.}}^{\text{Inlet}} (\text{mol}/\text{min}))} \times 100 \quad (9)$$

where n , is the number of all compounds detected at outlet including unreacted glycerol.

3. Results and discussions

3.1. Pre-design and pre-characterization for catalyst preparation

As aforementioned, three OMS (SBA-15, MCM-41 and KIT-6) were firstly synthesized. Their respective mass yield in SiO_2 (after calcination at 500 °C) were 71.5 %, 59 % and 56.9 %, as indicated by TGA analysis (Fig. S1 A). The conditions of preparation were adapted from the literature so that the total volume of pores (V_p) follows this order: SBA-15 (~1.49 cm^3/g) > MCM-41 (~1.06 cm^3/g) > KIT-6 (~0.77 cm^3/g), which has been measured by N_2 physisorption (Fig. S1 B-C). The objective was to examine the capacity of different OMS for hosting controlled-size nanoparticles of Mo species, because oxides of transition metals are mainly suffering from low surface per volume ratio, sintering and leaching, particularly when high loading of metals was used in hydrothermal medium [21,31,35,45]. Besides, existing nanosized porosity in OMS can lead to a good dispersion of Mo particles and more uniform sizes distribution. This architectural approach offers to evaluate how further geometrical exposure of Mo particles affects both the population of redox sites and their surface acidity, if actually relevant.

Secondly, the optimal content of Mo salt ($\text{H}_3\text{P}(\text{Mo}_3\text{O}_{10})_4 \cdot 12 \text{H}_2\text{O}$) to melt-infiltrate onto each OMS material was evaluated for SBA-15, which was chosen as model support. The in-situ DSC diagrams of bare Mo salt, and of six other samples involving increasing amount of Mo salt (from 0.06 to 1.64 g) previously melt-infiltrated inside 1 g of uncalled SBA-15 are plotted in Fig. 1A. The diagrams of mixed samples correspond to metal loading between 4.4 wt% and 55.8 wt% of Mo, estimated at its fully reduced state. This percentage was calculated based on the mass yield of SiO_2 expected to be obtained from the calcined SBA-15 material.

The in-situ DSC diagram of bare Mo salt shows a melting peak at ~81 °C, which is very close to the theoretical one (~79 °C). The other peaks at temperatures lower than 65 °C and higher than 90 °C reflect the elimination of humidity and structural H_2O , respectively. For Mo@SBA-15 mixtures, DSC diagrams clearly indicate a depressed melting point of Mo salt from 81 °C to lower temperature, indicating the effective melt-infiltration of Mo salt by capillary diffusion into SBA-15 pores. The

depressed peak is broad but with quasi-monomodal component that begins to appear from ~18 °C and then progressively shifts towards 40 °C as the added amount of Mo salt is increased. This indicates probably a progressive filling of small mesopores first and then of larger pores in which the capillary effect is usually less involved. This conclusion is in good agreement with the interpretation of N_2 isotherm and BJH profiles (Fig. S1 B-C), indicating the existence of mesopores in parent SBA-15, of which the diameter range is relatively broad (between 5.4 and 8.4 nm). Furthermore, the diffusion process of Mo salts is facilitated by the hydrophilic character of internal pores of SBA-15 that possess some Si-OH groups [57], while its outer surface and bulk framework are dominantly hydrophobic [46]. At higher Mo loading, the peak at 81 °C corresponding to the melting of bulk Mo salt reappeared, which is due to the Mo salt remaining on the outer surface of SBA-15. The melting enthalpy of this residual extra-porous salt and of the bulk Mo salt at 81 °C (56.4 J/g) were calculated to quantify the pore-filling degree of SBA-15 using Eq. 1 cited in Section 2.3. Fig. 2B plots the amount of Mo salt in the intra-pores of SBA-15 as a function of the amount of Mo salt added

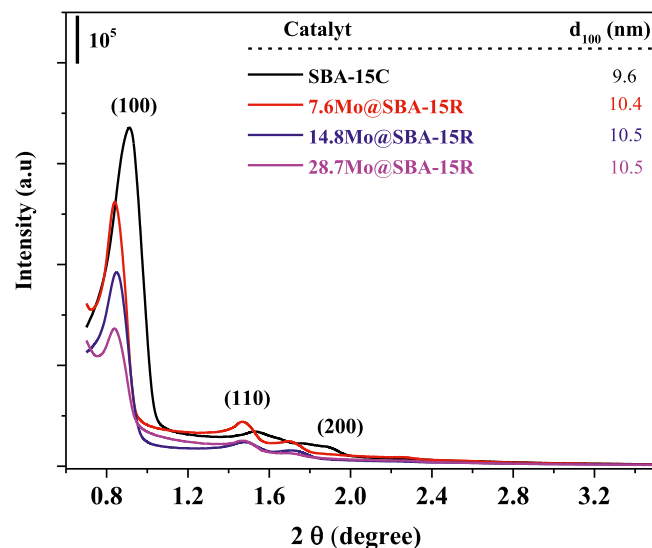


Fig. 2. Small-angle XRD diagrams of parent SBA-15 C calcined under air at 500 °C, and of hybrid Mo@SBA-15 R (with 7.6 wt%, 14.8 wt%, 28.8 wt% of Mo element) that have been reduced under H_2 -flow at 500 °C after being melt-infiltrated at 85 °C for three days. d_{100} (nm) stands for the intra-plane spacing of the (100) peak.

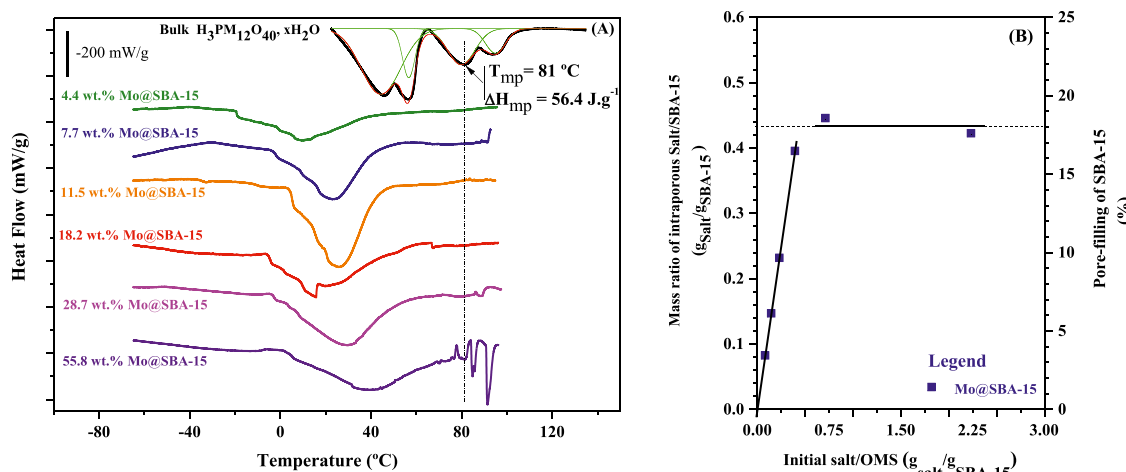


Fig. 1. In-situ DSC diagrams recorded for bare and for different amounts of $\text{H}_3\text{P}(\text{Mo}_3\text{O}_{10})_4 \cdot 12 \text{H}_2\text{O}$ salt melt-infiltrated into 1 g of SBA-15 support (A), and Plot of the intra-porous Mo amount effectively incorporated inside the pores volume of SBA-15 network (B).

initially. As observed, the pore-loading reached a plateau at $\sim 0.44 \text{ g}_{\text{salt}}/\text{g}_{\text{SBA-15}}$, which corresponds to $\sim 19.6 \text{ wt\%}$ of fully reduced Mo in the final catalyst. So, the maximum pore-fillings corresponded to 18 vol% of filled pore volume from SBA-15 which has a total volume of $1.49 \text{ cm}^3 \cdot \text{g}^{-1}$, as calculated by N₂-physisorption (Table in Fig. S1 B). This approximation was done considering that the intra-porous Mo salts maintain the same crystalline phase with an apparent density of $1.62 \text{ g} \cdot \text{cm}^{-3}$. Beyond this practical limit of pore-filling, it is unnecessary to increase the metals loading, since it will remain agglomerated and weakly anchored on the limited external surface of SBA-15, which will be easy to drag during the envisaged use in hydrothermal reaction medium.

To check the evolution of 3D structure of SBA-15 after pore-filling, small-angle X-ray diffraction was applied to bare SBA-15 and hybrid 7.7Mo@SBA-15, 14.8Mo@SBA-15 and 28.8Mo@SBA-15 samples, which have been previously melt-infiltrated at 85°C for 3 successive days. This temperature of diffusion was just slightly higher than the experimental melting point of Mo salt (81°C), but below its decomposition temperature ($\sim 95^\circ\text{C}$), as experimentally determined (Fig. 1 A). Besides, The diffusion time was optimized by in-house preliminary experiments to be three days to promote a homogeneous filling of SBA-15 pores (data not shown), which is in good agreement with the data reported by our group for similar metals [45]. The obtained small-angle X-ray diagrams are plotted in Fig. 2, where the (100), (110) and (200) reflections were clearly observed for all the samples. This is an indication that the hexagonal symmetry (*p6mm*) of ordered SBA-15 remained intact including at Mo loading higher than the limit suggested by in-situ DSC analyses. This suggests that the pore-walls of the prepared SBA-15 are sufficiently strong to support high Mo loading. It is also observed that intensity of the main peak (100) decreased as the Mo loading increased, which confirms the filling of pores by Mo particles. This pores' filling by metal provoke an increasing of the density of pores initially empty that becomes near to that of SiO₂ framework, thereby, suppressing the SBA-15 order-periodicity and diminishing the intensity of X-ray peaks [45]. In comparison with parent SBA-15, the main (100) peak is slightly shifted to lower 2θ in the melt-infiltrated Mo@SBA-15 samples, while the corresponding d_{100} (nm) spacing increased as Mo amount increase. This may reflect some expanding in the framework of silica since the pores filling effectively introduces a certain alteration in the local order of SBA-15 but without destructing its 3D structure. This suggests that the hybrid Mo@SBA-15 samples are stable and maintain a similar structure to that of the parent silica.

As a conclusion, small-angle X-ray diffraction and in-situ DSC data well-complement each other; precisely in confirming the good stability of silica framework and effective pores filling unveiling the maximal limit of Mo amount to incorporate onto OMS. This latter was determined at a level of occupation of 18% of the OMS total pores volume. Based on these preliminary insights, it was decided to incorporate a Mo loading equivalent to occupy only 3/4 of the available pores volume of SBA-15, MCM-41 and KIT-6 materials. This partial value was chosen to avoid any risk of blocking all the accessible porosity by an excess of Mo. This maximal loading of Mo corresponds to nominal values of 14.8 wt%, 11 wt% and 8.7 wt%, which is estimated based on the fully reduced state of Mo⁰ to incorporate in the total pore volume of each calcined OMS that has been previously measured by N₂ sorption (Fig. S1B-C).

3.2. Mo oxide-based catalysts and their physiochemistry

Based on the aforementioned preliminary insights, the target loading of MoO_x was incorporated onto SBA-15, MCM-41, and KIT-6 systems to compare them with impregnated MoFe/AC (chosen as a reference [21, 31]), bulk MoO_x and Fe/MoO_x catalysts. In some cases, some samples were pre-calced under air or pre-reduced under H₂ to check if MoO_x strongly interacts with SiO₂. Thus, the name of pre-calced samples was termed by C (i.e. MoO_x @SBA-15 C), while that of pre-reduced was termed by R (i.e. MoO_x @SBA-15R). The corresponding XRD diagrams

(Fig. S2) indicate that both treatments did not produce any silico-molybdates that are less reactive. However, calcination caused a pronounced sintering of MoO₃ (JCPDS N° 05–0508), leading to particles sizes between 27 nm and 61 nm, as estimated by the Scherrer model (Eq. 3). Also, it provokes sintering of the Fe₂(MoO₄)₃ phase (JCPDS N° 83–1701) formed by the interaction of FeO_x and MoO₃. After reduction, both Fe/MoO_x and MoO_x samples feature XRD diagrams with a predominant MoO₂ phase (JCPDS 86–0135), of which the sintered particles are between 42 nm and 56 nm, respectively. However, the reduction of the MoO_x @SBA-15R catalyst stabilizes a well-dispersed Mo particle (with sub-2 nm size) that is invisible in the XRD profile, while the pre-calcdination of MoO_x @SBA-15 C strongly sintered the Mo species (up to 27 nm). Furthermore, TGA analysis (Fig. S3) revealed that the pre-treatment of the Mo-based SBA-15 catalyst under a H₂ atmosphere formed carbonaceous species ($\sim 6.1 \text{ wt\%}$) by polymerizing the structure-directing agent used during the synthesis. These carbon fragments seem to slow down the mobility of transition metals towards agglomeration [53]. In fact, as we will see further on, the rest of the Mo-based OMS catalysts were pre-reduced under H₂ to improve the Mo dispersion. Table 2 shows detailed information in terms of elemental composition and textural, redox, as well as acid-sites properties of the studied Mo oxide-based catalysts.

ICP data show that the real mass loading of metals in all pre-calcdinated catalysts was in good agreement with the predicted nominal values. The deviation does not exceed $\pm 6\%$, which is in the range of the usually observed experimental error. However, the pre-reduced systems, MoO_x @SBA-15R, MoO_x @MCM-41R, and MoO_x @KIT-6R, present some more deviation (up to 18%), which could be attributed to the deposition of the carbon fragment during the reduction; 6.1 wt%, 8.1 wt%, and 7.3 wt%, respectively (Fig. S3). The presence of such species was also confirmed by CHNS measurements, where their content is between 3.51 wt% and 4.95 wt%. The difference between the mass values of the CHNS and TGA analyses suggests that these species are polymerized C_xH_y compounds rather than a purely graphitic-like carbon.

In terms of the textural properties (Table 2 and Fig. S4), bulk MoO_x and Fe/MoO_x feature a N₂ isotherm of intragranular materials, where their surface and pore volume do not exceed $83 \text{ m}^2/\text{g}$ and $0.08 \text{ cm}^3/\text{g}$, respectively. This is in line with the XRD insights, indicating the existence of sintered MoO₃ particles. It is well-reported that these oxides suffer from a low surface area and porosity [35]. However, the texture of the MoFe/AC catalyst is mostly set by the AC support, disposing of well-developed laminar structures. In turn, each MoO_x @OMS-based catalyst showed a N₂ isotherm similar to that of the bare OMS family (SBA-15, MCM-41, KIT-6) because the texture of the supported catalysts is mainly imposed by the support-type [17]. According to the IUPAC classification, MoO_x @OMS systems show a type IV (or mixed type IV + type I) N₂ isotherm, indicating the existence of remarkable mesoporosity with a minor part of micropores. Each isotherm shows a pronounced H₂ hysteresis, which is characteristic of OMS [45], confirming that meso-porosity is maintained after the incorporation of the Mo element. The catalysts based on SBA-15 and MCM-41 feature only mesopores, because during the synthesis of these supports, a single template; P₁₂₃ for SBA-15 and CATB (with C₁₉) for MCM-41, was used. Also, the crystallization of SBA-15 at temperature (in our case 105°C), which is higher than the cloud point of the P₁₂₃ surfactant (90°C), seems to have modified the mesophase of P₁₂₃ surfactant. Such temperature decreases the strength of the interaction between the P₁₂₃ surfactant and the inorganic matter, resulting in a densification of the walls and the formation of larger mesopores [45]. For MCM-41, we have used CTAB as surfactant (with alkyl chain of C₁₉ atoms) that led to the formation of typical mesopores of 2–3 nm [55]. To form micropores in MCM-41, organic surfactant with lower alkyl chain length (mainly with C_{<16}) should be used [55]. Moreover, comparing the texture of MoO_x @OMS catalysts (Table 1 and Fig. S4 C-D) with that of the bare OMS support (Fig. S1 B-C), we observe that only the SBA-15-based catalyst suffered from some decrease in the porosity. In fact, the distribution of their

Table 2

Nomenclature of Mo oxides-based catalysts and their main physicochemical properties.

| Catalyst | Loading wt% (*) | | | S _{BET} | V _p (Tot) | D _p (Large) | D _p (Narrow) | V _p | Acid-sites | Redox-sites |
|----------------------------|-----------------|----------|--------|-------------------|----------------------|------------------------|-------------------------|--------------------|---|---------------------------|
| | Mo | Fe | C | m ² /g | cm ³ /g | nm | nm | cm ³ /g | mmol (NH ₃)/g _{Mo} | mmol (CO)/g _{Mo} |
| FeMo/AC | 19.3(18.6) | 2.8(2.9) | (78) | 1285 | 1.21 | — | 3.8 | 0.14 | — | — |
| MoO _x | 66.6 (—) | — | — | 83 | 0.08 | — | 3.5 | 0 | 0.14 | 0.43 |
| Fe/MoO _x | 58.1 (54.6) | 8.9(8.8) | — | 81 | 0.08 | — | 3.7 | 0 | 0.11 | — |
| MoO _x @SBA-15 C | 14.8 (13.9) | — | — | 733 | 0.86 | 7.1 | 3.7 | 0 | 2.16 | 1.07 |
| MoO _x @SBA-15R | 14.8 (12.1) | — | (3.51) | 772 | 1.10 | 7.5/6.4 | — | 0 | 1.65 | 1.98 |
| MoO _x @MCM-41R | 11 (9.5) | — | 4.48 | 1070 | 0.98 | 0 | 2.6 | 0 | — | — |
| MoO _x @KIT-6R | 8.7 (7.3) | — | (4.95) | 735 | 0.74 | 5.0 | 3.7 | 0.07 | — | — |

wt% → Nominal weight loading of elements, while (*) stands their real loading determined by ICP or CHNOS. SBET → Surface area estimated by BET; V_p(Tot) → Total pore volume obtained at P/P₀ = 0.95; D_p(large) and D_p(narrow) → Average width of large and narrow mesopores, respectively, estimated by BJH model; V_p → Micropore volume estimated by "t-plot" method. Acid-sites → Total number of acid-sites quantified from NH₃-TPD profiles. Redox-sites → Number of partially reduced sites estimated by CO adsorption. — → Not determined.

pore-size becomes bimodal and less intense due to the pore filling by Mo nanoparticles. This decrease is more pronounced on the pre-calcined MoO_x @SBA-15 C, which may be due to the blockage of mesopores by larger MoO_x particles formed during the calcination, as revealed by XRD analysis. All of these insights thus confirm once again the existence of some pores filling by Mo particles for the SBA-15 catalyst, as initially revealed by in-situ DSC and X-ray scattering. However, the monomodal pore-size distribution of MCM-41 centered at 2 nm and the bimodal one centered at 3.7 nm and 5.1 nm for the KIT-6 support remain practically unchanged after Mo incorporation. This suggests that Mo species particles remain mostly located outside the pores of KIT-6 and MCM-41 materials.

In addition to these elemental and morphological differences, NH₃-TPD and in-situ CO-IR data from selected catalysts, MoO_x, Fe/MoO_x, MoO_x @SBA-15 C, and MoO_x @SBA-15R, also indicate remarkable differences in their acidity and redox properties.

As shown in Table 1 and Fig. S5, these four catalysts exhibit weak and mild acidity through two overlapped peaks of NH₃ desorption between 115 and 495 °C. MoO_x and Fe/MoO_x systems provide a low amount of acid-density, 0.14 mmol/g_{metal} and 0.11 mmol/g_{metal}, respectively. It is well reported [44,58] that MoO_x and FeO_x tend to exhibit mainly Brønsted sites related to their Mo-OH and/or Fe-OH termed. The small difference observed between both values may originate from the deposition of impregnated FeO_x species that block more acid Mo-OH centers [44,58]. The blockage of pores on Fe/MoO_x has been observed in the BJH profile (Fig. S4 B). On the other hand, the density of acid-sites was noticeably increased when MoO_x was dispersed onto SBA-15, i.e., 1.65 mmol/g_{Mo} for MoO_x @SBA-15R and 2.16 mmol/g_{Mo} for MoO_x @SBA-15 C. This acidity increase might be firstly caused by a more geometrical exposure of highly defected MoO_x species because the well-developed 3D structure of SBA-15 mainly induce further dispersion of metals [59]. Secondly, this acidity is more pronounced on the pre-calcined MoO_x @SBA-15 C catalyst, which implies that the pre-calcination under air might be responsible for further increasing the interfacial electrons transfer between MoO_x and SiO₂. This is supported by the fact that the SiO₂ matrix is inert towards NH₃ chemisorption [59], which means that the increase in the NH₃ uptake is essentially coming from the vacancy of SiO₂/Mo electron transfers.

In turn, in situ CO-IR data (Fig. S6 and Table 1) indicate that both bulk MoO_x and dispersed MoO_x @SBA-15 C and MoO_x @SBA-15R catalysts feature carbonyl species coordinated to Mo⁰(3 < φ ≤ 5) sites, exhibiting band frequencies between 2203 and 2257 cm⁻¹ that are higher than those of free or physisorbed CO at 2138 cm⁻¹. [53] This large frequency distribution is a signal of various oxidation-reduction degrees of Mo species. Quantitatively, MoO_x @SBA-15R features the highest density of CO-sites (1.98 mmol/g_{Mo}), which is practically 2 times higher than that of MoO_x @SBA-15 C (1.07 mmol/g_{Mo}) and 4.6 times higher than that of bulk MoO_x (0.43 mmol/g_{Mo}). This high density of CO sites can be attributed not only to the double reduction treatments

that mainly create Mo defects with an unsaturated oxygen coordination, acting as redox-sites [60], but also to the improved geometrical exposure of Mo nanoparticles, as previously evidenced by the XRD data. The carbon clusters on MoO_x @SBA-15R seem to significantly prevent the sintering of Mo nanoparticles. The existence of carbon has also been confirmed by the MS detector during the NH₃-TPD measurements as its thermal decomposition lead to overlapped peaks of CO_x and H₂O observed between 495 and 700 °C (Fig. S5).

3.3. Mo carbide-based catalysts and their physiochemistry

In view of the promising properties of MoO_x @SBA-15R, it was used to obtain the dispersed carbide phases, such as β-Mo₂C@SBA-15R and η-MoC@SBA-15R, in order to compare with bulk β-Mo₂C and η-MoC systems. The aim was to unveil how forming new Mo-C bounds affect the redox and acid characteristics of Mo species. The XRD diagrams (Fig. S7) of representative bulk carburized samples, prepared as described in Section 2.2, confirmed the formation of the β and η phases. The carbo-thermal treatment under CH₄/H₂ mixtures effectively leads to a well-dispersed β-Mo₂C phase (JCPDS 00-011-0608), while the treatment under C₃H₈/H₂ forms a η-MoC phase (JCPDS 01-089-4305) with a minor presence of MoO₂ (JCPDS 86-0135). In turn, β-Mo₂C@SBA-15R and η-MoC@SBA-15R exhibited broad XRD diagrams (not shown), which suggests that the β-Mo₂C and η-MoC phases are still invisible as sub-2 nm crystallites. The content of Mo and C in carbide-based catalysts and their main texture and the most significant redox and acid properties are summarized in Table 3 and illustrated in Figs. S8–10.

Thus, the mass loading of Mo was increased in the carburized bulk samples due to the exchange of heavy O atoms by light C atoms that represent less than 11.3 wt%. However, this Mo content was not greatly changed in the dispersed Mo carbides onto SBA-15 because SiO₂ is the major component (> 82 wt%). The surface areas and meso-porosity were significantly increased for bulk β-Mo₂C (457 m²/g, 0.45 cm³/g) and bulk η-MoC (220 m²/g, 0.25 cm³/g) samples in comparison with bulk MoO₃ samples (83 m²/g, 0.08 cm³/g). This is in good agreement with the XRD diagrams (Fig. S7), reflecting a dispersed carbide phase with broad diffraction peaks. Delporte et al. [61] reports that a reducing atmosphere mainly creates a structural defect in Mo species, which increases their surface area. Besides, the dispersed Mo carbides feature globally similar N₂ isotherms and BJH profiles to those of the MoO_x @SBA-15R counterpart. This is an indication that the initial well-developed porosity and 3D structure are still maintained despite the carburization treatment at high temperatures (590–700 °C) for extended times.

As a consequence of this further geometrical exposure, β-Mo₂C@SBA-15R exhibits a significant increase in the population of NH₃ sites (1.41 mmol/g_{Mo}) compared to bulk β-Mo₂C (0.17 mmol/g_{Mo}), as shown in Table 3 and Fig. 9. This acidity is also related to the creation of oxygen vacancies that act as acid-sites [60] and the relatively more

Table 3

Nomenclature of Mo carbides-based catalysts and their main physicochemical properties.

| Catalyst | Weight loading | | S _{BET} | S _{BET} | V _p (tot) | D _p (Large) | D _p (Narrow) | Acid-sites | | Redox-sites | |
|-----------------------------|----------------|-------|------------------|------------------|----------------------|------------------------|-------------------------|---|---------------------------|-------------|--|
| | wt% * | * | | | | | | mmol (NH ₃)/g _{Mo} | mmol (CO)/g _{Mo} | | |
| β-Mo ₂ C | 88.6 | 11.34 | — | — | 457 | 0.45 | — | 3.8 | 0.17 | 0.58 | |
| β-Mo ₂ C@SBA-15R | 9.3 | 4.97 | — | — | 941 | 1.12 | 5.2 | 3.8 | 1.41 | 1.15 | |
| η-MoC | 88.7 | 11.27 | — | — | 220 | 0.25 | — | 3.9 | — | — | |
| η-MoC@SBA-15R | 12.2 | 4.83 | — | — | 1319 | 1.52 | 5.1 | 3.7 | — | 1.35 | |

wt% * → Real weight loading of Mo determined by ICP and of C determined by CHNOS. SBET → Surface area estimated by BET; V_p(Tot) → Total pore volume obtained at P/P₀ = 0.95; D_p(large) and D_p(narrow) → Average width of large and narrow mesopores, respectively, estimated by BJH model; V_μ → Micropore volume estimated by “t-plot” method. Acid-sites → Total number of acid-sites quantified from NH₃-TPD profiles. Redox-sites → Number of partially reduced sites estimated by CO adsorption. - → Not determined.

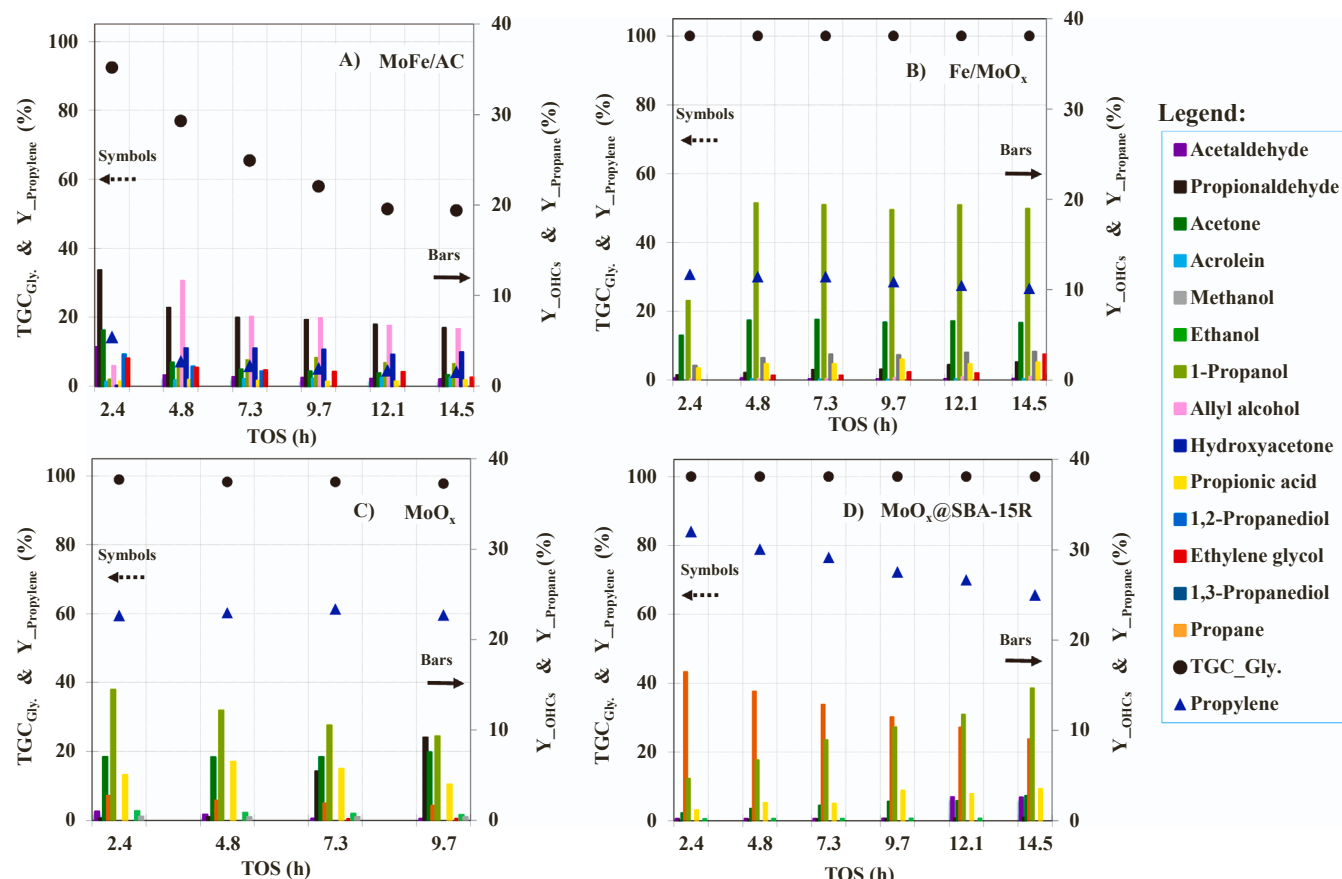


Fig. 3. Evolution of total glycerol conversion and of yields of propylene and co-products as function of time on stream for; A) MoFe/AC, B) Fe/MoO_x, C) bulk MoO_x and D) MoO_x @SBA-15R. tested in single-step HDO of glycerol/H₂O (10/90 wt%) at 318 °C, 50 bar, H₂/C₃H₈O₃ (mol.) = 98 and WHSV= 1.7 h⁻¹.

acidic characteristic of Mo-C bands. In turn, the population of CO sites follows the same trend. Thus, the dispersed β-Mo₂C and η-MoC phases inside SBA-15 contain about 1.15 mmol/g_{Mo} and 1.35 mmol/g_{Mo}, respectively, while the bulk β-Mo₂C shows just 0.58 mmol/g_{Mo} (Table 3, Fig. S10). Bulk β-Mo₂C shows two vibration bands at 2157 cm⁻¹ and 2138 cm⁻¹, corresponding to partially reduced Mo-CO and physically adsorbed CO, respectively [53], while β-Mo₂C@SBA-15R and η-MoC@SBA-15 feature additional shoulders at 2206 cm⁻¹ and 2175 cm⁻¹ (Fig. S10). This difference in bandings and number of CO-sites, which depend on the dispersion and carbide phases, suggests the presence of Mo sites with a different chemical environment. Stellwagen et al.[62] reported that sub-10 nm particles of Mo carbides increase their oxyphilic surface. In fact, the high dispersion of our sub-2 nm Mo particles might not only increase the population of CO-sites through more geometrical exposure but also induce an even

greater oxyphilic characteristic of Mo-C bands. This aspect is more pronounced on the η-MoC@SBA-15R catalyst, carburized via a transition topotactic route; MoO₃ → MoO₂ → MoO_xC_y and η-MoC. The existence of MoO_xC_y in carbide samples has been experimentally revealed [63], while DFT calculations indicated that these intermediates with sub-monolayer oxygen feature high oxophilicity [64].

3.4. Glycerol HDO on Mo oxide-based catalysts

As described earlier, all Mo oxide-based catalysts were firstly tested in a single-step HDO of glycerol/H₂O (10 wt%) at 318 °C and a pressure of 50 bar or 30 bar for TOS between 4.8 h and 14.5 h. Preliminary tests with a long time on stream (TOS) were performed first to check if it is possible to overtake the initial transition state of the catalyst to reach its stationary state. The molar ratio of H₂/glycerol and WHSV were set at 98

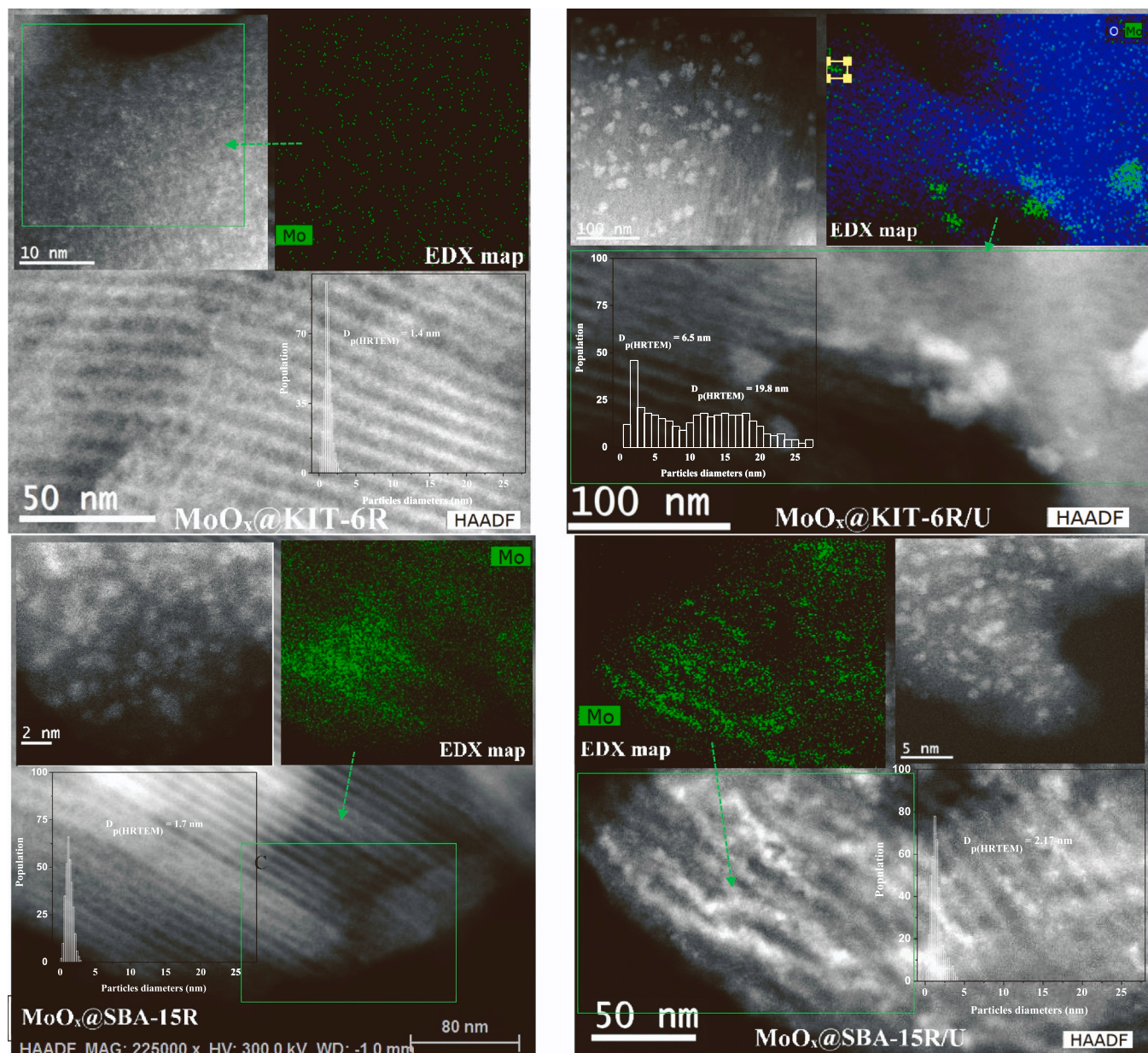


Fig. 4. High-resolution TEM-HAADF images at scale between 2 nm and 100 nm, which include the corresponding maps of STEM-EDX scanning and the histograms of Mo nanoparticles sizes distribution for fresh MoO_x @KIT-6R (top left) and used MoO_x @KIT-6R/U catalysts (top right), and for fresh MoO_x @SBA-15R (bottom left) and used MoO_x @SBA-15R/U catalysts (bottom right).

and 1.7 h⁻¹, respectively. These conditions correspond to a fully gas-phase reaction, as calculated by Aspen software (Fig. S11). Blank tests with an excess mass of bare SBA-15 mixed in inert SiC were also performed and repeated two times. For these blank tests, the conversion never exceeded 9.1%, where the mol of glycerol converted per mol of SiC/SiO₂ mixture during 1 h was much less than 1, which suggests a thermo-conversion of glycerol rather than a proper catalytic act. This confirms the inactivity of SiC and SiO₂ species used as the bed-diluent and support, respectively.

As for Mo oxide-based catalysts, they show a high catalytic reactivity, where the distribution of the arising products depends on the characteristics of the catalysts themselves and their testing conditions. The main products detected in the gas phase are propylene and propane, as well as volatile OHCs such as propionaldehyde, 1-propanol, acrolein, allyl alcohol, acetone, acetaldehyde, ethanol, and methanol. Very small amounts of ethylene, ethane, methane, and carbon dioxides were also detected. The condensed phase consisted of trapped volatiles and heavy

OHCs such as hydroxyacetone, 1,2-propanediol, 1,3-propanediol, propanoic acid, ethylene glycol, and non-converted glycerol. Table 4 summarizes the performance of all Mo oxide-based catalysts in terms of total glycerol conversion, deoxygenation, hydrogenation, and C-C breaking activities, as well as in terms of propylene yield and carbon balance. As these parameters sometimes decrease gradually after several hours in the reaction, the pseudo-first order constant of their deactivation rate was also included. In turn, Fig. 3 plots the temporal evolution of the total glycerol conversion and propylene and OHC yields of MoO_x @SBA-15R and bulk MoO_x catalysts in order to put in evidence their significant behavior compared to those of MoFe/AC (chosen as reference) and Fe/MoO_x catalysts.

For the MoFe/AC catalyst (with ~2.9 wt% Fe and ~18.6 wt% Mo), the conversion of glycerol decreases with time from 92.4% to 51.1%, leading to a positive constant of deactivation (~63.8 10⁻³ h⁻¹), while the propylene yield also decreases from 14.3% to 4.2%. The deactivation constants of the deoxygenation, hydrogenation, and reforming activity

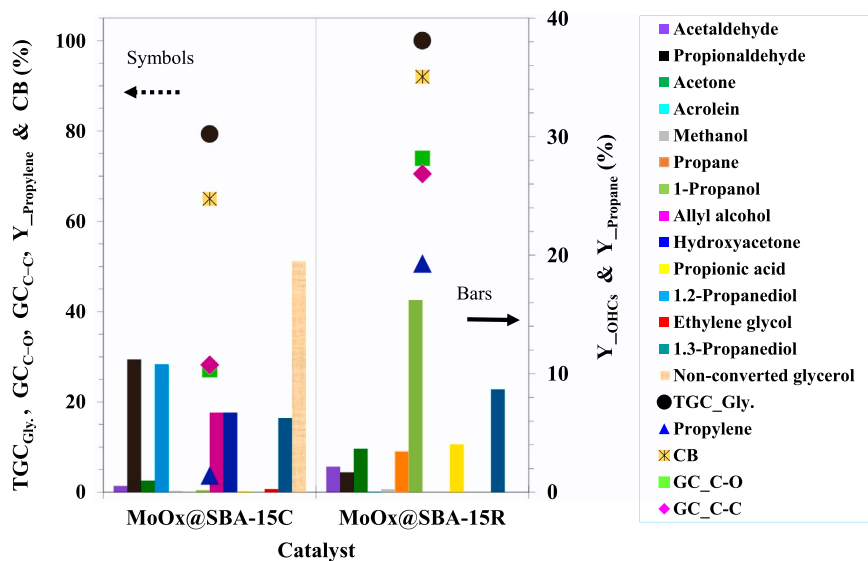


Fig. 5. Total conversion of glycerol, deoxygenation and hydrogenation activities, and yields of propylene and main OHCs obtained over MoO_x @SBA-15 C and MoO_x @SBA-15R catalysts, which were estimated at 4.8 h of reaction at; 318 °C, 30 bar of H_2 , $\text{C}_3\text{H}_8\text{O}_3/\text{H}_2\text{O}$ (10/90 wt%), $\text{H}_2/\text{C}_3\text{H}_8\text{O}_3$ (mol) = 98 and WHSV = 1.7 h^{-1} .

are also positive values; $68.6 \cdot 10^{-3} \text{ h}^{-1}$, $75.4 \cdot 10^{-3} \text{ h}^{-1}$, and $110.5 \cdot 10^{-3} \text{ h}^{-1}$, respectively. This tendency may be due to a diminution of active-sites mainly caused by easy sintering of metals impregnated on AC, as reported previously by Zacharopoulou *et al.* [22], [31]. It is a reasonable explanation because the surface of carbon contains less charges and develop low interaction with transition metals, thereby evolving to form larger particles that are easy to be agglomerated.

Bulk MoO_x catalysts provide full glycerol conversion and stable propylene yield at around 59.6%, where the main co-products are 1-propanol, propionaldehyde, acetone, propanoic acid, and propane. They also feature high and stable activity in deoxygenation (80.9%) and hydrogenation (66.9%) and a negligible activity in reforming (0.8%) to close the carbon balance at 95.7%. This high HDO activity is related to the high Mo content in bulk Mo oxides (~66.6 wt% Mo), where H_2 reduction leads to the creation of unsaturated MoO_{3-x} sites. [21], [38]. The stable behavior may be attributed to the larger initial particles of MoO_3 (~61 nm, Fig. S4) that are already thermodynamically stable and do not undergo further agglomeration. In turn, Fe/MoO_x catalysts (~8.8 wt% Fe and ~54.6 wt% Mo) provide just 26 % propylene yield, which is 2.3 times lower than that of MoO_x catalysts, despite their full glycerol conversion. They also feature minor activities in deoxygenation (58.9 %) and hydrogenation (68.7 %) that forms rather more partially deoxygenated C_3 molecules such as 1-propanol, acetone, and propanoic acid. Wan *et al.* [34] reported that the addition of FeO_x can reduce the oxophilicity of MoO_x species, which consequently minimizes their tendency to interact with oxygenate intermediates. This can be related to the formation of $[\text{Fe}_2\text{MoO}_3]_4$ crystallites, as indicated by our XRD data (Fig. S2), whereas the H_2 treatment was not sufficient in completely reducing the FeO_x nanoparticles, thus subtracting the certain availability of Mo sites for HDO events. In summary, an adequate availability of Mo sites with rich-vacancy defects is necessary for improving the HDO of glycerol and its intermediates to form more propylene rate.

Thus, the MoO_x @SBA-15R catalyst (with a high dispersion of just 14.8 wt% of Mo) features an unprecedented almost quantitative yield of fully deoxygenated C_3 molecules (~84 % propylene and ~15 % propane) at full glycerol conversion, while the yield of liquid oxygenates is insignificant. However, despite the fact that the conversion of glycerol remains total, the yield of propylene and propane slightly decreases with TOS progresses down to 65.6 % and 9.1 % after under 14.5 h stream, respectively. This decreasing tendency was accompanied with a proportional increase in the yield of 1-propanol, propanoic acid, and acetone. This proportional exchange in the yield of products does not

cause a significative decrease in its deoxygenation and hydrogenation activities, whereas the deactivation rates stay moderate at $14.9 \cdot 10^{-3} \text{ h}^{-1}$ and $7 \cdot 10^{-3} \text{ h}^{-1}$, respectively. However, an appreciable increase in the activity of C-C breaking to form $\text{C}_1\text{-}\text{C}_2$ molecules, mainly acetaldehyde, ethylene, ethane, and very little CO_2 , was observed, which manifests itself through a high negative value of the rate constant ($-110.7 \cdot 10^{-3} \text{ h}^{-1}$). This slight deviation in the reaction route may be related to a certain change in the redox sites that represses the deoxygenation and hydrogenation events while concurrently amplifying the acidic cracking rate. The NH_3 -DTP profile of the used MoO_x @SBA-15R sample (Fig. S.12) revealed that the density of acid-sites increased up to 1.94 mmol/g_{Mo}, which is 17.7% higher than that of the fresh sample, i.e., 1.65 mol/g_{Mo}. This acidity increase usually arises from the appearance of new -OH groups over MoO_x species after interacting with the H_2O of the medium or oxygenates intermediates. Nonetheless, the GTP route largely remains the main catalytic route.

In turn, the pre-calcined MoO_x @SBA-15 C catalyst features a glycerol conversion of 96.3 % with notably less activity in deoxygenation (43.5%) and hydrogenation (40.1 %, Table 4). Propionaldehyde is the main product whereas the yield of propylene decreased from 30.8% to 12%, as shown in Fig. S13. In fact, the deactivation rates for C-O cleavage ($56.1 \cdot 10^{-3} \text{ h}^{-1}$), C-C hydrogenation ($56.6 \cdot 10^{-3} \text{ h}^{-1}$), and C-C breaking ($164.6 \cdot 10^{-3} \text{ h}^{-1}$) are more pronounced compared to those of the MoO_x @SBA-15R catalyst. This behavior may be related to the decreased availability of Mo sites with HDO abilities. The CO chemisorption data support this explanation because the density of redox-sites is practically two times lower in MoO_x @SBA-15 C than in MoO_x @SBA-15R. It seems that the pre-calcination under air, which caused some sintering of the Mo surface (see XRD data in Fig. S2), induces further electron transfer between MoO_x and SiO_2 . This interaction may contribute to lowering of the reducibility of Mo oxides, which usually occurs with transition metals [65]. Also, the NH_3 -TPD data (Table 1 and Fig. S9) indicate the high acid density on MoO_x @SBA-15 C that may increase the formation of oxygenates by direct dehydration (i.e., glycerol to acrolein, etc.). For example, the gradual increase in the acrolein yield during the last hours of reaction (Fig. S13), which is accompanied by a proportional decrease in the propionaldehyde yield, can also be related to some suppression of hydrogenation events of acrolein to propionaldehyde. However, further details about the contribution of the redox/acidity ratio could be the object of a separate study in the future.

Regarding the MoO_x @MCM-41R and MoO_x @KIT-6R catalysts, they showed the worst stability despite their good initial catalytic activity

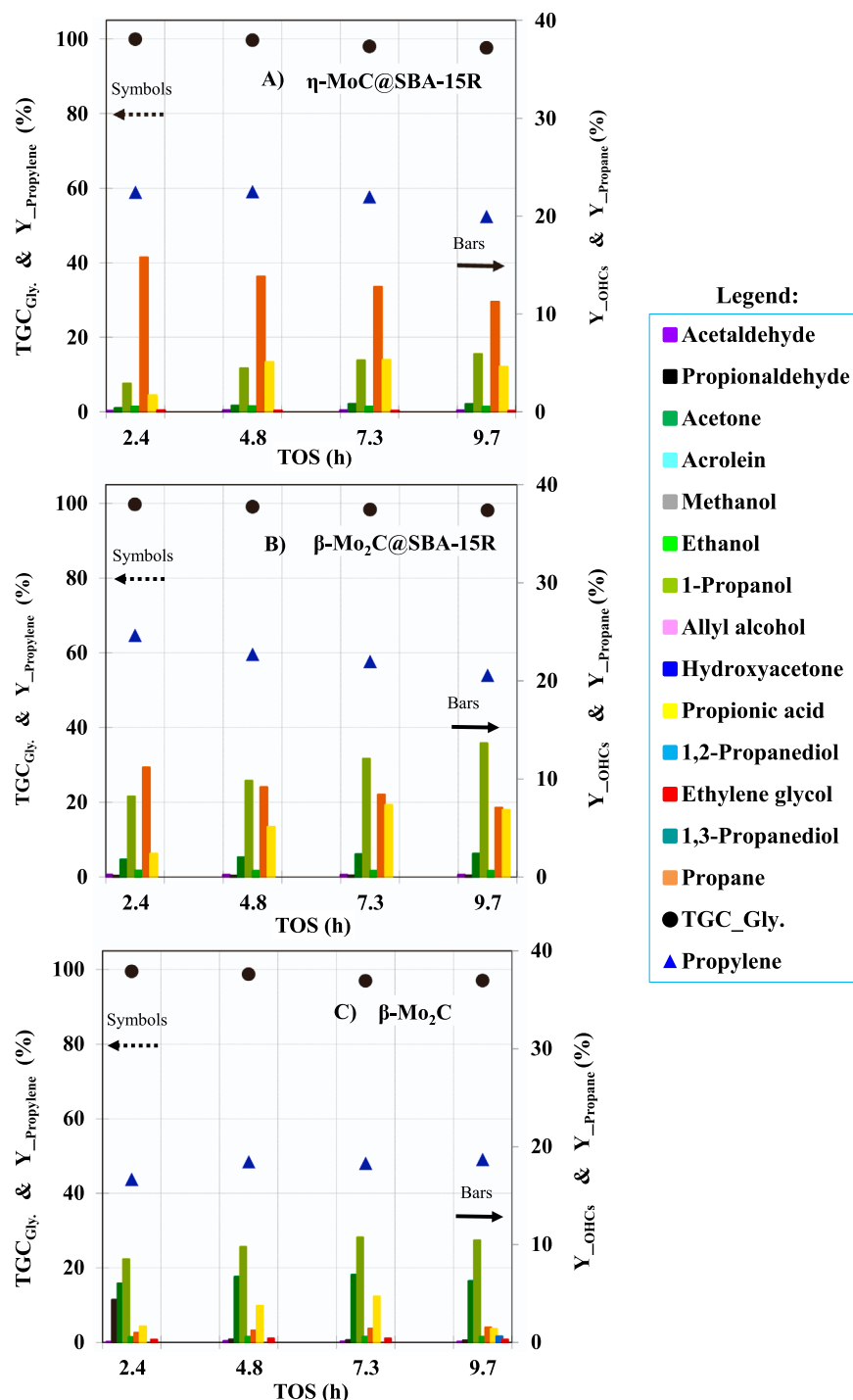


Fig. 6. Evolution of total glycerol conversion and of yields of propylene and co-products as function of time on stream for; A) bulk η -MoC@SBA-15R, B) β -Mo₂C@SBA-15R, and C) β -Mo₂C catalysts tested in single-step HDO of glycerol/H₂O (10/90 wt%) at 318 °C, 50 bar, H₂/C₃H₈O₃ (mol.) = 78, WHSV = 2.35 h⁻¹, and TOS of 9.7 h.

and selectivity towards propylene (Table 4 and Fig. S13). At the beginning of the test, they featured a total glycerol conversion of 100% and 96%, respectively, but after 14.5 h of reaction, both values were drastically decreased to only 24.6% and 53.5%, respectively. Their respective propylene yield follows the same trend, decreasing from 48.5% and 52.1% to only 2.1% and 7.1%, respectively. Also, the deoxygenation, hydrogenation, and reforming activities follow the same trend, where the corresponding constants of deactivation provide high positive values of 242.4 10⁻³ h⁻¹, 202.4 10⁻³ h⁻¹, and 155.6 10⁻³ h⁻¹, respectively, for the MoO_x @MCM-41R catalyst, and 182.6 10⁻³ h⁻¹,

164.510⁻³ h⁻¹, and 195.310⁻³ h⁻¹, respectively, for the MoO_x @KIT-6R catalyst. Consequently, the yield of oxygenates, mainly hydroxyacetone, propionaldehyde, allyl alcohol, and ethylene glycol, also decreased, which suggests that both the surface quality and number of sites were greatly changed during the reaction. These changes could emerge from a possible evolution of Mo species or of the silica support itself.

Normally, MCM-41 is well known for its narrow mesopores (~ nm) [46] that could have further prevented the melt-infiltration of Mo particles inside the pores, thus, leaving them on the outer surface suffering

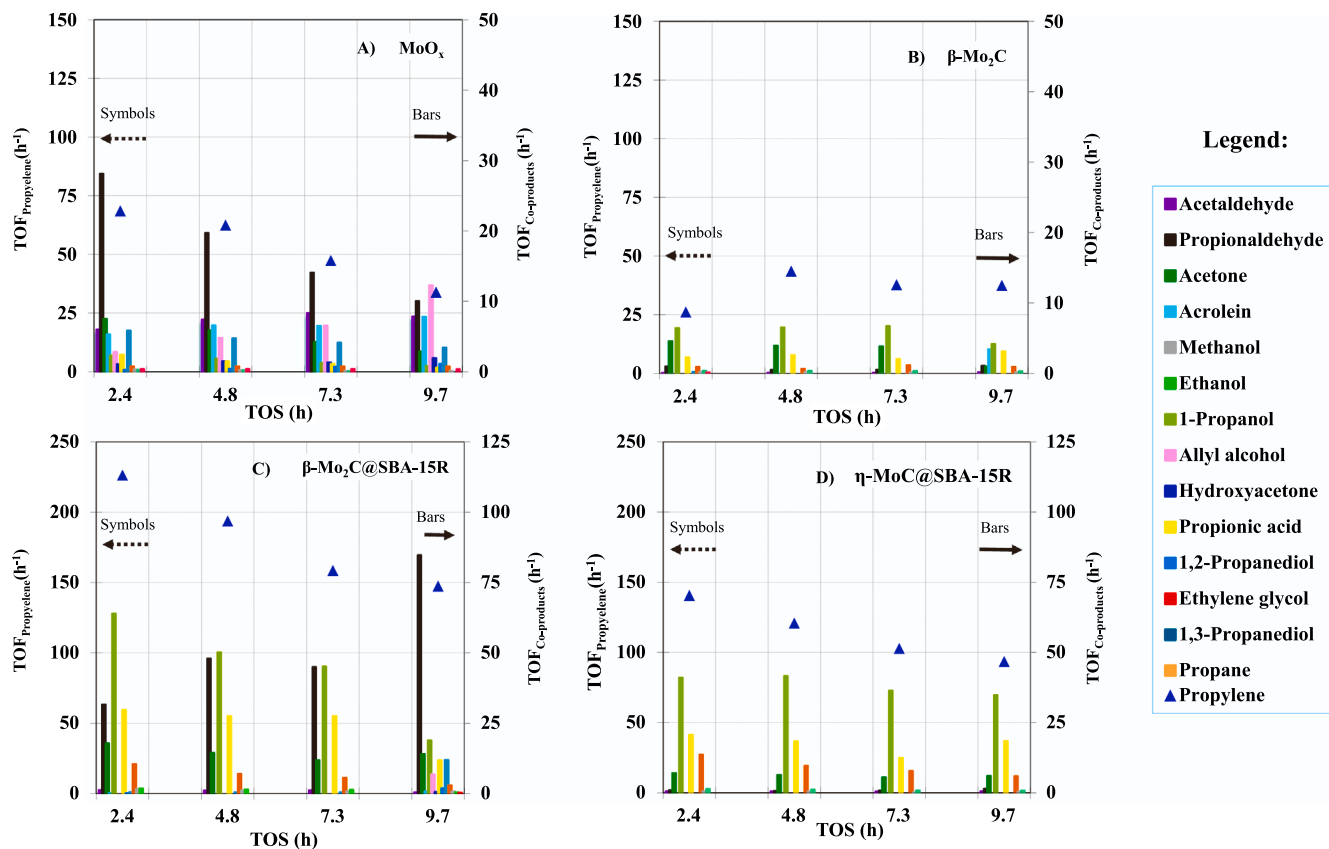


Fig. 7. Evolution of TOF of propylene and co-products as function of time on stream for; A) bulk MoO_x , B) $\beta\text{-Mo}_2\text{C}$, C) $\beta\text{-Mo}_2\text{C}@\text{SBA-15R}$ and D) $\eta\text{-MoC}@\text{SBA-15R}$ catalysts tested in single-step HDO of glycerol/ H_2O (10/90 wt%) at 318 °C, 50 bar, $\text{H}_2/\text{C}_3\text{H}_8\text{O}_3$ (mol.) = 78 and WHSV = 4.7 h^{-1} .

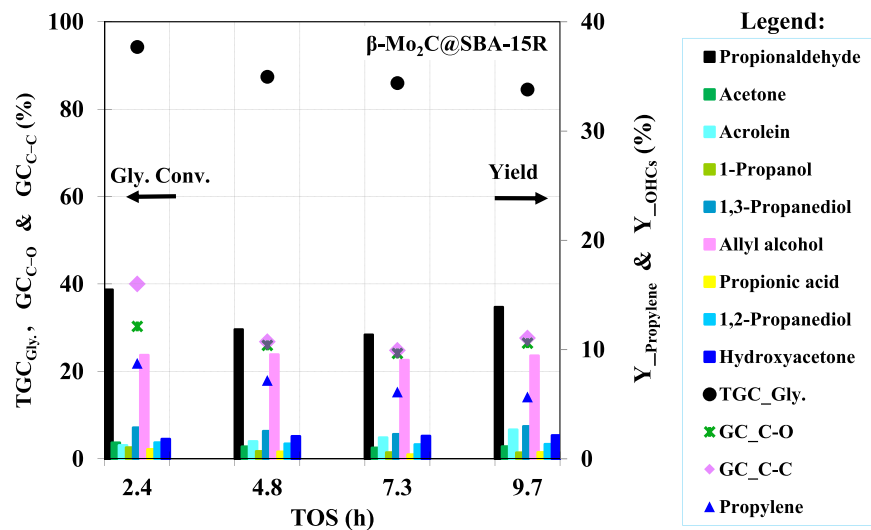


Fig. 8. Evolution of glycerol conversion, deoxygenation and hydrogenation activities (primary axis, left), and the yields of propylene and co-products (secondary axis, right) for $\beta\text{-Mo}_2\text{C}@\text{SBA-15R}$ tested in liquid-phase HDO conditions of glycerol/water (10/90 wt%) at 264 °C, 50 bar, $\text{H}_2/\text{C}_3\text{H}_8\text{O}_3$ (mol.) = 78, WHSV = 2.35 h^{-1} and TOS = 9.7 h.

from a quick agglomeration. Also, it is well-known that MCM-41 features a nonexistent interconnectivity between their neighboring meso-channel,[46] which makes them unstable materials in a hydrothermal medium. Concerning the MoO_x @KIT-6R catalyst, comparative high-resolution TEM-HAADF images of selected fresh and used samples (Fig. 4) effectively confirm the evolution of the MoO_x and KIT-6R morphologies. The fresh sample shows more superficial dispersion of

Mo nanoparticles over KIT-6R, where the histogram of their average size distribution is monomodally centered at 1.4 nm. However, this good Mo dispersion was strongly changed after reaction towards larger agglomerates, resulting in a broad geometrical distribution of Mo particles with bimodal histograms centered at around 6.5 nm and 19.9 nm. This could be caused by a partial structural fall of the KIT-6 framework during the reaction because some distortion in the used KIT-6 structure was

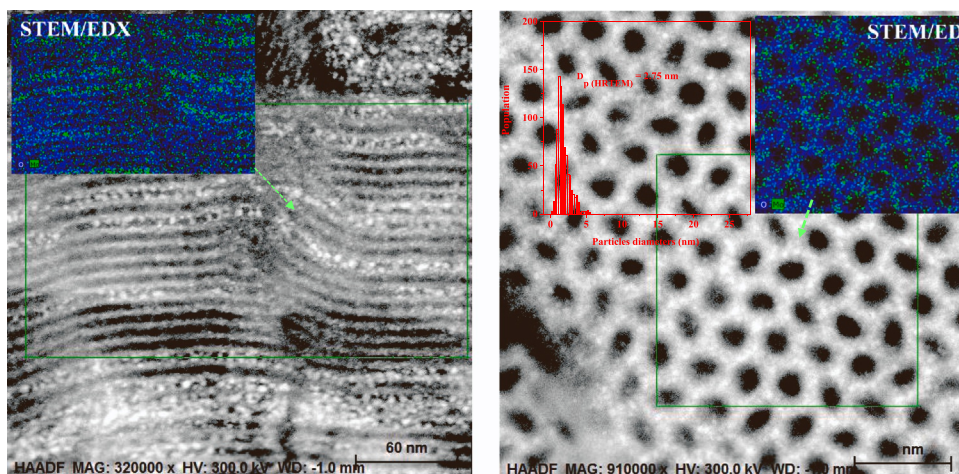


Fig. 9. Representative TEM-HAADF images at scale between 20 nm (right) and 60 nm (left), which include the corresponding maps of STEM/EDX scanning and the histogram of Mo nanoparticles sizes distribution for used β -Mo₂C@SBA-15R catalysts tested at 318 °C, 50 bar, C₃H₈O₃/H₂O = 10 wt%, H₂/C₃H₈O₃ (mol)= 78, WHSV= 4.7 h⁻¹ and TOS = 9.7 h.

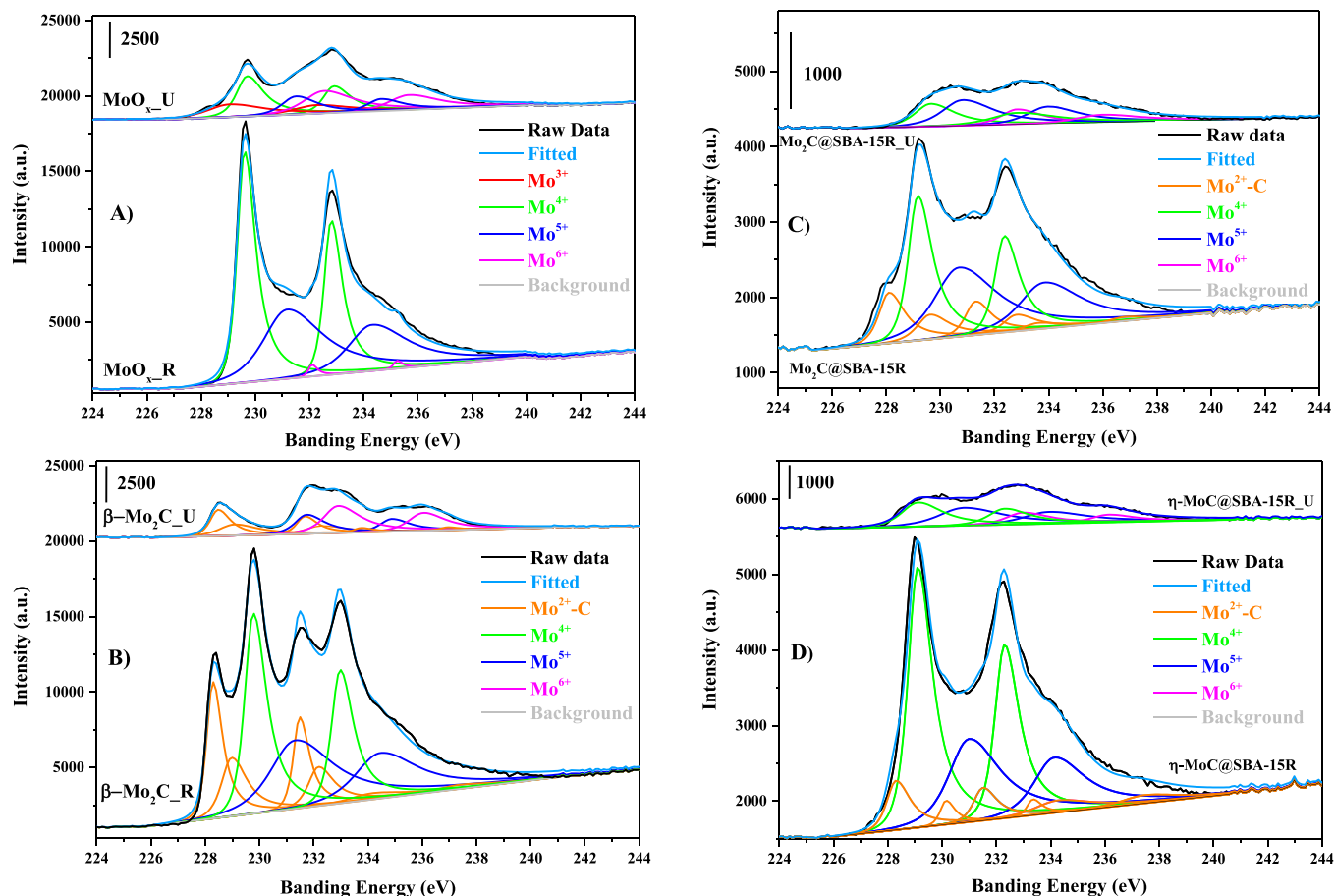


Fig. 10. High-resolution XPS spectra of Mo3d core-level and their deconvolution for fresh and used bulk MoO_x (A) and β -Mo₂C (B), and dispersed β -Mo₂C@SBA-15R (C) and η -MoC@SBA-15R (D) catalysts. All systems were tested at same glycerol/water mixture (10/90 wt%), T = 318 °C and P = 50 bar. However, H₂/C₃H₈O₃ molar ratio, WHSV and TOS were; 98, 1.7 h⁻¹ and 14.5 h, respectively, for bulk MoO_x; 78, 2.35 h⁻¹ and 9.7 h, respectively, for bulk β -Mo₂C; and 78, 4.7 h⁻¹ and 9.7 h, respectively, for dispersed β -Mo₂C@SBA-15R and η -MoC@SBA-15R catalysts.

observed (Fig. 4). KIT-6 aged at a low 85 °C habitually develops a thin and insufficient interconnectivity between its meso-channels, which gives it a frail silica framework; vulnerable to being destroyed in a H₂O-rich medium. As consequence of all these changes, the number of accessible active sites might have significantly decreased on MoO_x

@MCM-41R and MoO_x @KIT-6R catalysts to convert glycerol and oxy-genes, thus resulting in an evident deactivation.

The MoO_x @SBA-15R catalyst features, however, very good morphological and structural stabilities, as confirmed by TEM-HAADF images of fresh and used samples (Fig. 4). Thus, sub-2 nm MoO_x

Table 4

Total glycerol conversion, and deoxygenation, hydrogenation and reforming activities, and their pseudo-first order deactivation constant, as well as propylene yield and carbon balance provided by Mo oxides-based catalysts tested in single-step HDO of glycerol. Test conditions: 318 °C, 50 bar, C₃H₈O₃/H₂O = 10/90 wt. %, H₂/C₃H₈O₃ (mol)=98.7 and WHSV=1.7 h⁻¹ for TOS of 14.5 h.

| Catalyst | TGC _{gly} (%) ^a [K _{TGC_{gly}} .10 ³ (h ⁻¹)] | GCC-o (%) ^a [K _{GCC-o} .10 ³ (h ⁻¹)] | GCC-c (%) ^a [K _{GCC-c} .10 ³ (h ⁻¹)] | GC _{c-/c} (%) ^a [K _{GC_{c-/c}} .10 ³ (h ⁻¹)] | Y _{C₃H₆} (%) ^a | CB(%) ^a |
|---------------------------|---|--|--|---|--|--------------------|
| MoFe/AC | 51.1 [63.8] | 19.9 [68.6] | 24.1 [75.4] | 2.2 [110.5] | 4.4 | 80.1 |
| Fe/MoO _x | 100.0 [0.0] | 58.9 [13.1] | 64.7 [6.3] | 4.6 [-28.6] | 26.1 | 79.7 |
| MoO _x | 98.0 [1.7] | 80.9 [5.1] | 66.9 [10.9] | 0.8 [81.1] | 59.6 | 95.7 |
| MoO _x @SBA-15R | 100.0 [0.0] | 91.0 [14.9] | 74.6 [7.0] | 1 [-110.7] | 65.6 | 105.1 |
| MoO _x @SBA-15C | 95.6 [2.8] | 43.5 [56.0] | 40.1 [56.6] | 0.7 [164.6] | 12.0 | 75.6 |
| MoO _x @MCM-41R | 24.6 [318.3] | 8.7 [242.4] | 12.8 [202.4] | 0.3 [155.6] | 2.1 | 91.2 |
| MoO _x @KIT-6R | 53.5 [75.3] | 24.8 [182.6] | 24.7 [164.5] | 0.2[195.3] | 7.1 | 82.6 |

^a Parameters calculated at steady-state by taking an average value of GC analysis data (at last 1.5-3 hours of test).

particles are clearly observed in the fresh sample, where their size distribution is symmetrically centered at around 1.7 nm. EDX mapping clearly showed that these thin particles were mostly formed inside pores and arranged along uniform meso-channels, which is characteristic of SBA-15. The size of these channels (~ 8 nm) is of the same order of magnitude as that already indicated by the BJH model (Table 1 and Fig. S4). The visual filling of these mesopores confirms our preliminary insights obtained from in-situ DSC and X-ray scattering. Moreover, the TEM-HAADF images of used MoO_x @SBA-15R showed that both the Mo particle sizes (~2.1 nm) and their monomodal distribution remain similar to those of the fresh sample. Also, the hexagonal array of SBA-15 remains unchanged after the reaction. This good morphological stability of MoO_x @SBA-15R can be explained by the synthesis protocol. The aging of the starting mixture for the SBA-15 synthesis at around 105 °C usually makes the as-synthesized SBA-15 develop an optimal compromise between the opening of the meso-pores and the resistance of the silica walls/thickness [45,66]. This silica with enough strength enables the hosting of a high loading of Mo nanoparticles and facilitates the diffusion of the reactant and products, which explains, in a certain way, the better stability of the MoO_x @SBA-15R catalyst, including under harsh hydrothermal conditions. The slight decrease in the yield of propylene along TOS (Fig. 3) could be related to some re-oxidation of partially reduced Mo^{δ+} species, as we will see further on. However, the small evolution of the Mo particle sizes from 1.7 nm to 2.2 nm does not seem to significantly change the surface of the catalyst.

So, seeing that MoO_x @SBA-15R and MoO_x @SBA-15 C catalysts dispose of inverted redox and acid properties, they were also tested at a lower total pressure (30 bars). As shown in Fig. 5, the MoO_x @SBA-15R catalyst features better HDO performance than that of MoO_x @SBA-15 C, although it is less than those obtained at 50 bars. MoO_x @SBA-15R maintains full conversion and yields more hydrogenated molecules, mainly propylene, propane, and 1-propanol, which are a result of its high deoxygenation and hydrogenation activities, 74% and 70.5%, respectively. However, MoO_x @SBA-15 C provides just 79% of the total glycerol conversion, which is mainly to less hydrogenated OHCs such as propionaldehyde, acrolein, allyl alcohol, hydroxy-acetone, 1,3-propanediol, and unconverted glycerol. The difference in their HDO activity can be correlated to the density of redox and acid sites in each catalyst. However, their lower catalytic performance compared to that obtained at 50 bars can be explained by the lower H₂ availability at reduced total pressure of 30 bars. Actually, when decreasing the total pressure from 50 to 30 bars, the partial H₂-pressure decreases consequently from 35 to only 18 bars. Thus, H₂ adsorption becomes insufficiently activated, which negatively affects the regeneration of redox-sites that are necessary to further accomplish the hydrogenation events and maintain the high C-O cleavage activity. Recent DFT calculations[38] indicated an effectively high energy barrier for H–H dissociation over MoO₃, whose values are 1.46–1.63 eV depending on the configuration of the -OH formed. In fact, the creation of the oxygen vacancy through the H* reaction with neighboring surface O is kinetically decelerated

despite the energy of the global process being only 0.30 eV. This lower regeneration of the oxygen vacancy could be offering a greater possibility of the intervention of acid-sites, thereby deviating the reaction towards dehydration pathways. This effect is more pronounced in MoO_x @SBA-15 C, which provide a greater NH₃-site/CO-site ratio (~2.02) due to its pre-calcination under O₂/N₂ (20/80 vol%). In fact, this acid catalyst forms more OHGs and exhibits very lower selectivity towards further hydrogenated molecules such as propylene and propane. This is exactly the opposite for the MoO_x @SBA-15R catalyst (with a low NH₃-site/Co-site ratio of ~0.83), which was pre-reduced under pure H₂, that shows a significant selectivity towards further hydrogenated molecules (i.e., propylene, propane, and 1-propanol). In conclusion, the high HDO rate of the MoO_x @SBA-15R catalyst can be ascribed to its robust activity in C-O breaking and C-C hydrogenation induced by its high density of redox-sites, while the extent of the deoxygenation-hydrogenation of the MoO_x @SBA-15 C catalyst seems to be repressed by its pronounced acidic characteristic.

Regarding the lower performances of both catalysts at 30 bars compared to those at 50 bars, the thermodynamics may also be playing an unfavorable role, thus negatively affecting the propylene yield at a lower total pressure. According to the Le Châtelier rules [67], when the total pressure is decreased, the reaction will shift towards more molecules in the gas phase. In our case, it will favor the reaction pathways that repress the consumption of H₂ or at least those that consume less moles of H₂ (used in excess) to maintain the high number of moles of gas, thus partially rewarding the effect of decreasing the pressure. Concretely, HDO of glycerol theoretically needs two or three moles of H₂ to be fully deoxygenated in one mole of propylene or propane, respectively. However, certain partially dehydrated compounds (i.e., acrolein, C₃ diols, allyl alcohol, etc.) can be formed via dehydration without external H₂ consumption or via hydrogenolysis with just one mole of H₂, which maintain high number of moles in gas-phase at lowing the total pressure. It is thus concluded that increasing the H₂ pressure is evidently preferred to favor the pathways of single-step GTP. However, a reasonable ratio of H₂/glycerol vis-a-vis glycerol/H₂O ratio should be optimized because: i) excessive H₂-pressure can further hydrogenate the C=C band of propylene into C-C bands in propane, ii) high partial pressure of H₂O would cause excessive re-oxidation of partially reduced Mo^{δ+} sites, and iii) use a minimal of external H₂ is also good for the economy of GTP process.

Finally, it should be noted that a carbon balance close to 100 % (Table 4) was observed on the catalysts, MoO_x @SBA-15R and MoO_x, that feature high HDO activity in forming more hydrogenated gaseous products. However, a slightly lower carbon balance between 75.6% and 91.2% was observed on the remaining Mo oxide-based catalysts that strenuously form more liquid oxygenates. This may be due to the chemical instability of these OHC intermediates (i.e., acrolein, propionaldehyde, etc.) that rapidly undergo further oligomerization to undetectable compounds. Furthermore, the trapped solution provided by some catalysts was initially yellow to slightly brown. Its successive

injection in the GC, separated by various days, indicated effectively a slight evolution of their concentration but without detecting any oligomers, which can be due to incompatible GC's column (Stabiliwax) used for these experiments.

3.5. Glycerol HDO on Mo carbide-based catalysts

To study the effect of carburization on the stability of highly reactive Mo nanoparticles, the performance of Mo carbide-based catalysts was evaluated under more relevant HDO conditions. Thus, the temperature was set depending on the case at 264 °C or 318 °C and total pressure at 50 bars, which corresponds to a fully liquid or gas-phase reaction, respectively (Fig. S11). Also, the molar ratio of H₂/glycerol was decreased to 78, while the space-velocity was increased to 2.35 h⁻¹ and then to 4.7 h⁻¹. Table 5 summarizes the kinetic data estimated at the end of TOS for bulk β-Mo₂C, β-Mo₂C@SBA-15R, and η-MoC@SBA-15R catalysts. The performance of the bulk MoO_x catalyst tested at 4.7 h⁻¹ was also included for comparison purposes.

Thus, despite the fact that the space-velocity of the test was increased to 2.35 h⁻¹ and the molar ratio of H₂/glycerol was decreased to 78, all tested carbides, i.e., bulk β-Mo₂C and dispersed β-Mo₂C@SBA-15R and η-MoC@SBA-15R, feature full glycerol conversion and relatively stable activities in C-O deoxygenation (63.9 %, 74.6 %, and 76.8 %, respectively) and C-C hydrogenation (53.8 %, 64.1 %, and 62.7 %, respectively), while their activity in C-C breaking is insignificant. Any decreasing rate was not observed, and thus, the pseudo-first order deactivation constant is null. This performance resulted in a relatively stable propylene yield not only on bulk β-Mo₂C (at 49.1 %) but also on the dispersed β-Mo₂C@SBA-15R and η-MoC@SBA-15R catalysts at about 54 % and 55 %, respectively (Fig. 6). This suggests that the dispersed carbodic Mo sites are more catalytically stable than oxidic Mo sites dispersed on MoO_x@SBA-15R (Fig. 3). Besides, the dispersed Mo carbides feature robust HDO activity, where the distribution of products on β-Mo₂C@SBA-15R and η-MoC@SBA-15R includes mostly fully deoxygenated products (i.e., propylene and propane) with a total yield of 71 % and 65.1 %, respectively, which are much higher than those observed on bulk β-Mo₂C (50.3 %). The latter bulk carbide trends parallelly to form appreciated yields of oxygenates mainly; 1-propanol, acetone, and propanoic acid. This trend is in close agreement with literature [62], which reported that nanoparticles of Mo carbides tend to have an oxyphilic character, thus strongly interacting with the oxygen of glycerol and intermediates. The good hydrogenation activity, which is more pronounced in the η-MoC@SBA-15R catalyst, can be ascribed to the presence of a residual monolayer of MoO_xC_y [68], which has been justified previously in Section 3.2.

When the space-velocity was further increased to 4.7 h⁻¹, bulk β-Mo₂C, β-Mo₂C@SBA-15R and η-MoC@SBA-15R catalysts are being providing full glycerol conversion, however, bulk MoO_x catalyst reaches just 93 % of conversion. The three catalysts also show a good activity in deoxygenation (53.4 %, 50.8 %, and 43.9 %, respectively) and

hydrogenation (40.8%, 45.3%, and 39.9%, respectively), which are much better than those of bulk MoO_x catalyst (Table 5). Comparing the performance of bulk MoO_x and β-Mo₂C catalysts, it is clear that the carburization of Mo-O to Mo-C bands improves both the extent of HDO activities and the resistance to deactivation. In fact, β-Mo₂C catalyst provides constant propylene yield at 43.2%, which is 2 times higher than that of MoO_x catalyst. The propylene yield of this later decreases progressively to reach only 21.1%. This can be ascribed to the high density of redox-sites on bulk β-Mo₂C (0.58 mmol/g Mo), which seem emerge from the increased surface area of β-Mo₂C (457 m²/g) compared to that of MoO_x (83 m²/g). In turn, the further HDO activities of dispersed β-Mo₂C@SBA-15R and η-MoC@SBA-15R catalysts (with just 9.3 wt% and 12.2 wt% of Mo content, respectively) are manifested through the good initial yield of propylene that slightly decreases with TOS to reach a steady-state value of 31.0% and 32.1% after 9.7 h under stream, respectively. The relatively low values of the pseudo-first order deactivation constant of C-O cleavage and C-C hydrogenation activities for the β-Mo₂C@SBA-15R and η-MoC@SBA-15R catalysts indicate that the loss in HDO events does not severely accentuated.

To better visualize the aforementioned observations and to accurately identify what is the most active Mo phase for glycerol HDO and propylene formation, the specific activity in terms of TOF, namely, the mole of glycerol converted to propylene and each co-product per hour per CO-site on MoO_x, β-Mo₂C, β-Mo₂C@SBA-15R, and η-MoC@SBA-15R catalysts, is plotted in Fig. 7.

For bulk MoO_x catalyst, the TOF of propylene and of propionaldehyde decreases gradually with time from 68.2 h⁻¹ to only 33.7 h⁻¹, whereas those of allyl alcohol and acrolein trend to increase proportionally. This tendency is an indication that both the quality and the robustness of the catalytic site are changing with TOS to have less hydrogenation capacity under these conditions. Some researchers [69] report direct generation of allyl alcohol from glycerol, claiming a glycerol transfers hydrogen to acrolein to form allyl alcohol, which becomes incapable of further hydrogenation into propionaldehyde and then to propylene. However, for β-Mo₂C, the catalytic behavior becomes notably stable to form more hydrogenated products, mainly propylene and 1-propanol, and their TOF remains practically constant at 40.6 h⁻¹ and 6.7 h⁻¹, respectively. This stability per-site is an indication that no preferential loss of reactivity is occurring with time, which suggests that the carbodic site is catalytically different than oxidic sites. This can be related to the increase in the almost metallic character of Mo-C bands on the β-Mo₂C catalyst because there is a consensus that the hybridization of s/p-orbitals of the C atom with the d-orbital of the Mo atom tends to expand the d-band, approaching the electronic behavior of noble metals. [36] When β-Mo₂C or η-MoC was dispersed onto SBA-15, the TOF of propylene was multiplied to reach, at steady-state, 153.1 h⁻¹ and 98.2 h⁻¹, respectively, which are at least 3.8 and 2.4 times, respectively, higher than those provided both by the bulk β-Mo₂C or bulk MoO_x catalyst. Besides, the carbide Mo-C sites, particularly those on β-Mo₂C@SBA-15R to a lesser extent those on η-MoC@SBA-15R, feature

Table 5

Total glycerol conversion, and deoxygenation, hydrogenation and reforming activities, and their pseudo-first order deactivation constant, as well as propylene yield and carbon balance provided by carbides-based catalysts tested in single-step HDO of glycerol. Test conditions: 318 °C, 50 bar, C₃H₈O₃/H₂O = 10/90 wt. %, H₂/C₃H₈O₃ (mol)=78, WHSV=2.35 h⁻¹ and 4.7 h⁻¹ for TOS of 9.7 h.

| Catalyst | WHSV (h ⁻¹) | TGC _{gly} (%) * [K _{TGC_{gly}} · 10 ³ (h ⁻¹)] | GC _{C-O} (%) * [K _{GC_{C-O}} · 10 ³ (h ⁻¹)] | GC _{C-C} (%) * [K _{GC_{C-C}} · 10 ³ (h ⁻¹)] | GC _{C-C} (%) * [K _{GC_{C-C}} · 10 ³ (h ⁻¹)] | Y _{C₃H₆} (%) * [K _{Y_{C₃H₆}} · 10 ³ (h ⁻¹)] | CB (%) * [K _{CB} · 10 ³ (h ⁻¹)] |
|--------------------------|----------------------------|---|---|---|---|---|--|
| MoO _x | 2.35 | - | - | - | - | - | - |
| | 4.70 | 93.9 [5.0] | 39.4 [68.5] | 34.5 [65.5] | 1.3 [52.9] | 21.1 | 84.6 |
| β-Mo ₂ C | 2.35 | 99.5 [~ 0.0] | 63.9 [~ 0.0] | 53.8 [~ 0.0] | 0.7 [~ 0.0] | 49.1 | 82.1 |
| | 4.70 | 98.1 [3.3] | 53.4 [17.9] | 40.8 [32.9] | 0.3 [4.3] | 43.2 | 70.1 |
| β-Mo ₂ C@SBA- | 2.35 | 98.2 [~ 0.0] | 74.6 [~ 0.0] | 64.1 [~ 0.0] | 0.4 [58.9] | 54.0 | 91.2 |
| 15R | 4.70 | 96.3 [5.4] | 50.8 [58.1] | 45.3 [55.5] | 0.2 [116.3] | 31.0 | 83.9 |
| η-MoC@SBA- | 2.35 | 99.9 [~ 0.0] | 76.8 [~ 0.0] | 62.7 [~ 0.0] | 0.3 [63.1] | 55.1 | 85.6 |
| 15R | 4.70 | 99.9 [~ 0.0] | 43.9 [54.7] | 39.9 [50.5] | 0.2 [59.8] | 32.1 | 77.9 |

* Parameters calculated at steady-state by taking an average value of GC analysis data (at last 1.5-3 hours of test). - → not determined.

robust activities in C-O deoxygenation and C-C hydrogenation under these conditions. More specifically, the Mo-C sites of dispersed β -Mo₂C phase is more active and selective towards propylene formation, while those of the dispersed η -MoC one seems to have a slightly better hydrogenating character that is much better than those of Mo-O sites. This difference in their HDO robustness is clearly evidenced via the difference in their capacity to form fully deoxygenated and more hydrogenated compounds (i.e., propylene, propane) per site.

The improved HDO efficiency of the β -Mo₂C@SBA-15R and to a lesser extent η -MoC@SBA-15R catalysts, compared to those of bulk β -Mo₂C and MoO_x, can be also related to their high density in term of redox-sites, as indicated by IR-CO chemisorption (Table 3 and Fig. 10). However, the total TOF of propylene + propane tends to slightly decrease with time for both catalysts from 236.8 h⁻¹ to 155.8 h⁻¹ on β -Mo₂C@SBA-15R and from 154.2 h⁻¹ to 103.9 h⁻¹ on η -MoC@SBA-15R. In parallel, a proportional increasing in propionaldehyde yield; from 31.6 h⁻¹ to 84.7 h⁻¹ and from 0.9 h⁻¹ to 1.5 h⁻¹, respectively, was observed. This suggests that the carbide sites on dispersed catalysts, β -Mo₂C@SBA-15R and -MoC@SBA-15R, also undergo certain deactivation and thus become less hydrogenator for propionaldehyde to 1-propanol and then to propylene and finally to propane. This trend is less pronounced on the site of the η -MoC@SBA-15 catalyst, which features a more robust hydrogenation capacity to form more saturated propane, as mentioned above. From this analysis, we can conclude that the reductive-carburization of Mo-O sites to Mo-C significantly improves their catalytic activity and stability in C-O cleavage and C-C hydrogenation under hydrothermal conditions, including when the high space-velocity of glycerol was used. The stability improvement is more pronounced on the bulk β -Mo₂C catalyst, while the HDO robustness is remarkably higher on the dispersed β -Mo₂C@SBA-15R and η -MoC@SBA-15R catalysts, generating further propylene and propane per site.

To provide a comparative summary with the most relevant GTP performance reported so far, data from recent literature [21,22,24–29, 31,70,71] are shown in Table 7. It appears that the configuration of the GTP process is evolving from combined multi-steps reactions to continuous single-step HDO strategy. This latter seems to be more suitable for mass production of propylene. Thus, considering the relevance of GTP operating conditions particularly reaction steps, space-velocity and/or H₂/glycerol molar ratio, it seems that our single-step GTP performance over Mo-based catalysts is more promising than the majority of the previous works [21,24–29,31,70,71] and at least comparable with those of Fadigas et al. [22]. The propylene yield obtained in our study can reach values up to ~84.1 %, depending on the space-velocity (1.7 h⁻¹ to 4.7 h⁻¹) and the molar ratio of H₂/glycerol (78/1–98/1). However, Fadigas et al. used higher H₂/glycerol molar ratios (~120:1) to reach ~90% propylene selectively and ~100% glycerol conversion at space-velocity ~5.4 h⁻¹. The difference in propylene formation at similar space-velocity can also due to the high content of Mo and Fe metals (~28.7 wt%) in AC support, while our Mo-based catalyst contains only ~14.8 wt% of Mo. Regarding the other GTP performance, for example Wan et al. [29] and Sun et al. [28], reported propylene selectivity of 88% and 84.8 %, respectively, at H₂/glycerol (mol.) ~ 100:1, but they used space-velocity of only 1 h⁻¹ and 0.07 h⁻¹, respectively. Moreover, both studies combined a complex mixture of catalysts; WO₃(9.3 wt%)/T317 + SiO₂-Al₂O₃[28] and MoO₃/Ni₂P (20 wt%)/Al₂O₃ + ZSM-5 [29], respectively, in a double-bed reactor to reach such propylene selectivity. These complex mixtures of catalysts with less defined active-sites would make difficult their in-situ regeneration, since the mentioned selectivity is reported for only 2–5 h. According to the employed configuration, which involves two tandem reaction zones [26–29], the global GTP route is occurring through successive reactions with different kinetic rates. Thus, if the GTP reaction is extended for a longer time, some active sites may be deactivated before others. These drawbacks would negatively affect the operability of such multi-step strategy, which converts the single-step

Table 6

Banding energy of the most existing Mo ^{$\delta+$} species and their relative composition, and the interfacial atomic ratio of C/Mo and O/Mo elements for in-situ reduced (fresh) and post-reaction MoO_x, β -Mo₂C, β -Mo₂C@SBA-15R and η -MoC@SBA-15R (used) catalysts. All systems were tested at same glycerol/water mixture (10/90 wt%), T = 318 °C and P = 50 bar. However, H₂/C₃H₈O₃ molar ratio, WHSV and TOS were; 98, 1.7 h⁻¹ and 14.5 h, respectively, for bulk MoO_x; 78, 2.35 h⁻¹ and 9.7 h, respectively, for bulk β -Mo₂C; and 78, 4.7 h⁻¹ and 9.7 h, respectively, for β -Mo₂C@SBA-15R and η -MoC@SBA-15R catalysts.

| Catalyst | Mo ^{$\delta+$} species *Atomic ratio | B.E. (eV)_Fresh | B.E. (eV)_Used |
|---|---|---------------------------|----------------------|
| | | Mo 3d _{5/2} (eV) | Mo 3d _{5/2} |
| MoO_x | Mo ²⁺ -C | - | - |
| | Mo ³⁺ | - | 228.9 (20) |
| | Mo ⁴⁺ | 229.6 (50) | 229.7 (30) |
| | Mo ⁵⁺ | 231.2 (48) | 231.5 (17) |
| | Mo ⁶⁺ | 232.1 (2) | 232.5 (33) |
| | C/Mo | 0.01 | 7.67 |
| | O/Mo | 2.82 | 3.71 |
| β-Mo₂C | Mo ²⁺ -C | 228.3 (32) | 228.4 (40) |
| | Mo ³⁺ | - | - |
| | Mo ⁴⁺ | 229.8 (35) | - |
| | Mo ⁵⁺ | 231.3 (33) | 231.7 (22) |
| | Mo ⁶⁺ | - | 232.9 (38) |
| | C/Mo | 0.52 | 10.95 |
| | O/Mo | 2.23 | 5.92 |
| β-Mo₂C@SBA-15R | Mo ²⁺ -C | 228.1 (23) | - |
| | Mo ³⁺ | - | - |
| | Mo ⁴⁺ | 229.3 (34) | 229.6 (31) |
| | Mo ⁵⁺ | 230.8 (43) | 230.8 (45) |
| | Mo ⁶⁺ | - | 232.8 (25) |
| | C/Mo | 1.10 | 25.42 |
| | O/Mo | 31.19 | 50.79 |
| η-MoC@SBA-15R | Mo ²⁺ -C | -228.3 (16) | - |
| | Mo ³⁺ | - | - |
| | Mo ⁴⁺ | 229.1 (50) | 229.2 (37) |
| | Mo ⁵⁺ | 230.9 (34) | 230.8 (43) |
| | Mo ⁶⁺ | - | 232.9 (20) |
| | C/Mo | 1.29 | 73.57 |
| | O/Mo | 26.75 | 54.00 |

() → Surface atomic percent of different Mo ^{$\delta+$} species.

C/Mo and O/Mo → Interfacial atomic ratio of carbon and oxygen per molybdenum calculated based on the relative sensitivity factors of Wagner.

2 ≤ δ + 6 → Stands the oxidation state of Mo species.

GTP route over Mo-based catalyst in a promising alternative. Finally, it should be noted that a detailed discussion on GTP catalysis will be included in our next review, where the last mechanistic and engineering GTP's findings will be systematically confronted and contextualized within state-of-the art GTP literature to fill existing gaps and postulate future research trends.

Given that the β -Mo₂C@SBA-15R catalyst provides a promising TOF in propylene formation, it was also tested under liquid-phase HDO of glycerol at 264 °C and 50 bars because it is interesting from an economic point of view. Fig. 8 plots the temporal evolution of the conversion of glycerol, deoxygenation and hydrogenation activities, as well as the yields distribution of propylene and of the main co-products. Despite these unfavorable thermodynamic conditions, β -Mo₂C@SBA-15R remains highly reactive, as shown by its capacity to convert glycerol which starts from 94.3% and reaches 84.5% at steady state. It features low deoxygenation and hydrogenation activities at 27.6%, forming mainly mono- and bi- OHCs such as propionaldehyde, allyl alcohol, acrolein, hydroxy-acetone, and C₃ diols, while the propylene yield does not exceed 8.8%. An unrepresentative yield (< 0.1%) of C₁-C₂ co-products (i.e., acetaldehyde, ethylene glycerol, ethanol, and ethylene) was observed without CO_x detection, which confirms that the β -Mo₂C@SBA-15R catalyst is inactive towards C-C breaking, including under liquid-phase conditions. However, a low carbon balance (64%) was obtained in this test, which can be related to the instability of highly reactive intermediates or undetectable compounds.

Table 7

Summary of a selection of the most recent GTP performance as a function of operating conditions, catalyst type and reactor configuration.

| Ref.; year | Catalyst type and beds configuration | Main operating conditions | Conv. (%) | Sel. (%) | Yield (%) |
|------------------------------|--|--|-------------------|-------------|---|
| [25]; 2014 | Three staged fixed-beds; H-ZSM-5 (1 g), Pd (1 wt%)/γ-Al ₂ O ₃ (1 g) and H-BEA (0.5 g) | T~ 500 °C, 300 °C, 500 °C, P~ 1 bar, F _{H2} ~ 0.5 L/min, F _{N2} ~ 1.5 L/min, F _{Ar} ~ 0.2 L/min, gly. in H ₂ O~ 10 wt%, Feed~ 40 μL/min, WHSV~ h ⁻¹ , TOS~ 0.16–2.67 h | – | – | C _{2–3} olefins ~46*, ~15** |
| [26]; 2014 | Combined batch and fixed-bed; Ir (1 wt%)/ZrO ₂ (2 g) + HZSM-5–30 (2 g) | T~ 250 °C, P~5 bar-bar, H ₂ :gly. (mol.)~ 100:1, gly. in H ₂ O~ 3 wt%, WHSV~ h ⁻¹ , TOS~ h | 73 | 88 | – |
| [28]; 2015 | Double fixed-beds; WO ₃ (9.3 wt%)/T317(1 g) + SiO ₂ Al ₂ O ₃ (3 g) | T~ 250, P~ 1 bar, H ₂ ~ 180 mL/min, gly. in H ₂ O~ 20 wt%, Feed~ 1.32 mL/h, WHHSV~ 0.07h ⁻¹ , TOS~ 2–h | 100 | 84.8 | – |
| [27]; 2016 | Two-staged beds; Pt/ZSM-5(Si/Al~15, 1 g) + ZSM-5 (Si/Al~127, 1 g) | T~ 250 °C, 500 °C, P~ 1 bar, H ₂ :gly. (mol.)~ 100:1, partial pressure of gly. ~1.0 kPa, CH ₃ OH~1.2 kPa, H ₂ O~2.2 kPa, and H ₂ ~95.6 kPa, WHHSV~ h ⁻¹ , TOS~ 500 h | 100 | 63.7 | – |
| [22]; 2016 | Fixed-bed; MoFe (28.7 wt%)/Activated carbon, Fe/(Mo+Fe)~0.32 | T~ 300 °C, P~ 1 bar, H ₂ :gly(mol.)~ 120:1, gly. in H ₂ O ~ 90 vol.%, WHHSV~ 5.4 h ⁻¹ , TOS~ 24 h | 100 | 90 | – |
| [29]; 2017 | Double fixed-beds; MoO ₃ modified Ni ₂ P (20 wt%)/Al ₂ O ₃ + ZSM-5 | T~ 250 °C, H ₂ : gly (mol.)~ 100:1 | 100 | 88 | – |
| [21], [31], [71]; 2015, 2018 | Batch-bed; Fe (2.7 wt%)-Mo (19.3 wt%)/Black Carbon, (Mo/Fe ~4:1) | gly. in methanol ~ 59 wt%, WHHSV ~ h ⁻¹ , TOS~ h T~ 300 °C, P~ 80 bar, H ₂ : gly (mol.)~ 53:1, gly. in H ₂ O ~ 2wt.%, CT~ 7.2h, TOS ~ h | 88.8 | 76.1 | – |
| [24]; 2019 | Single fixed-bed; Fe (2.5 wt%) ZSM-5 | T~ 450 °C, P~ 1 bar, F _{N2} ~ 100 mL/min, gly. in H ₂ O ~ 10 wt%, Feed~ 0.4 mL/h, TOS~ 5 h | 100 | – | 33.3 |
| [70]; 2021 | Single fixed-bed; NiMoS _x /Al ₂ O ₃ (130 mg) | T~ 400 °C, P~ 18.6 bar, H ₂ excess, gly. in H ₂ O~72.5–80 wt%, CT~ 360 s, TOS ~ h | 100 | 26.3 | – |
| [72]; 2021 | Single Batch; Homogeneous Ru-complex (583 mg) | T~ 210 °C, P _{H2} ~40 bar, P _{CO} ~10 bar, H ₂ excess, pure glycerol, CT~ 285s, TOS ~ h | – | – | 57 |
| This work; 2022 | Single fixed-bed; MoO _x (14.8 wt%)@SBA-15 β-Mo ₂ C(14.8 wt%)@SBA-15 | T~ 318 °C, P~ 50 bar, gly. in H ₂ O~1 wt%, H ₂ :gly (mol.)~ 98 : 1, WHHSV ~ 1.7 h ⁻¹ , TOS~ 14.5hH ₂ :gly (mol.)~ 78:1, WHHSV~ 2.35 h ⁻¹ , TOS~ 9.7 h H ₂ :gly (mol.)~ 78:1, WHHSV~ 4.7 h ⁻¹ , TOS~ 9.7 h | 100 100 100 | – – – | ~84.1–65.6 ~64.8–54.0 TOFC ₃ H ₆ ~226.4–153.1 h ⁻¹ |

* Separated three-step reactions, ** Combined three-staged reactors, Conv. → conversion of glycerol, Sel. → selectivity of propylene, Yield → Yield of propylene → wt. → weight content, T → temperature, P → pressure, F_i → flow of gas, gly. → glycerol, WHHSV → weight hourly space velocity, CT → contact time, TOF → Turnover-Of Frequency, TOS → time-on-stream.

In view of the low yield of propylene at the high glycerol conversion of the β-Mo₂C@SBA-15R catalyst, it seems that this lower propylene selectivity is related to the unfavored effect of thermodynamics rather than to the lower reactivity of the catalyst. At 264 °C and 50 bars, both water and glycerol is in a full liquid phase, as evidenced by the Aspen calculation (Fig. S11), which affects the solubility of H₂[72] that is necessary to accomplish the hydrogenation events to form more hydrogenated propylene. Thus, we conclude that to work in a fully liquid phase, the H₂ pressure should be increased at an optimized temperature. This will allow the suppression of the reactions pathways that lead to the formation of partially deoxygenated co-products. However, this increase in pressure should be proportional to the temperature of the reaction to avoid excessive saturation of C=C of propylene bands to C-C of propane. Detailed optimization of the operating reaction conditions will be separately addressed in future work.

So far, no research has made a comparison of the single-step GTP reaction in the liquid and gas-phase as it is still particularly challenging to catalyze a hydrogenation reaction in a fully liquid phase and under a continuous-flow of H₂-pressure. However, it is very interesting to down with this defiance to highlight the advantages of liquid single-step GTP route regarding the other reaction strategies. To mention a few: i) working in a liquid phase using a single fixed-bed reactor can greatly reduce the installation volume and cost, ii) a low-temperature reaction limits both the degradation of biomolecules and the energy consumption due to unnecessary water evaporation, iii) a moderate pressure could be easily used in-situ for subsequent separation of propylene using well-developed membrane technologies or pressure swing adsorption. These beneficial characteristics could greatly improve the techno-economic viability of producing green propylene from bioglycerol.

3.6. Causes of HDO activity loss and active-site requirement for GTP reaction

In an attempt to investigate the causes of the slight decreasing HDO activity and propylene yield with time over the dispersed Mo-based catalysts, which were observed particularly at increasing space-velocity, chosen fresh and post-reaction catalysts (with relevant catalytic behavior) were examined by HRTEM-STEM/EDX and in-situ XPS techniques.

Fig. 9 displays high-resolution HAADF images, which include the corresponding STEM/EDX mapping and the histogram of the Mo particle size distribution, for the post-reaction β-Mo₂C@SBA-15R catalyst tested at 318 °C, 50 bars, and WHSV = 4.7 h⁻¹ for 9.7 h. These images clearly visualize a high density of longitudinal arrangement of Mo nanoparticles mostly located inside the pores and on the walls, where the hexagonal symmetry of SBA-15 remains intact despite the thermo-carburization at 700 °C and the test in a H₂O-rich reaction medium (90 wt%). EDX spectra (Fig. S14) recorded on this zone of pores confirms a Mo loading of ~12.9 wt%, which is in the same order as the nominal value (14.8 wt %) and to the real content measured by ICP (9.3 wt%), thus confirming that Mo leaching did not take place. The monomodal histogram of the Mo particle size distribution centered at 2.7 nm indicates that the geometry of particles does not suffer significant changes compared with that of the fresh MoO_x@SBA-15R catalyst initially centered at 1.7 nm (Fig. 4). The stability observed both for Mo nanoparticles and SBA-15 support rules out the sintering of Mo or the destruction of the 3D framework of SBA-15. These tangibles findings demonstrated the effectiveness of searching for hydrophobic OMS; specifically, SBA-15 with highly resistant silica walls and mesopores, to repel excessive H₂O adsorption, thus, protecting the hosted Mo nanoparticles against leaching and sintering, usually occurring under such hydrothermal

reaction medium ($\text{H}_2\text{O} \sim 90$ wt%, temperature and pressure) [22,31]. However, it remains to give further insights on how the different reduction-oxidation degree of Mo species, previously revealed by in-situ CO-IR spectra, have evolved along the reaction.

Thus, Fig. 10 shows a comparison between the $\text{Mo3d}_{3/2}$ - $\text{Mo3d}_{5/2}$ spin-orbit components of in-situ H_2 -reduced (fresh) and post-reaction MoO_x , $\beta\text{-Mo}_2\text{C}$, $\beta\text{-Mo}_2\text{C@SBA-15R}$, and $\eta\text{-MoC@SBA-15R}$ catalysts (used). Table 6 also summarizes the banding energy (BE) and chemical states of the most existing $\text{Mo}^{\delta+}$ ($2 \leq \delta + \leq 6$) species, which were enumerated based on the reported surface science [42,73]. The Mo composition and C/Mo and O/Mo atomic ratios were also included in an effort to find a correlation between the surface change and loss of HDO performance.

As mentioned in the characterization procedure (Section 2.3), Mo^{6+} , Mo^{5+} , Mo^{4+} , and Mo^{3+} were deconvoluted as one set of doublet peaks. However, $\text{Mo}^{2+}\text{-C}$ consists of three sets of doublets, where the first peak is strongly asymmetric, and the seconds are minors that correspond to an unscreened environment. The change of BE, intensity, and area of the Mo3d peaks from fresh and post-reaction samples were compared with those of the C1s, O1s, and Si2p core levels peaks. These spectral treatments and their interpretation offered a consisted deduction of the most active species for selective HDO of glycerol to propylene. Novel explanation for the loss of the HDO performance during the reaction were discussed.

Thus, the fresh MoO_x catalyst, which was in-situ reduced, features $3d_{5/2}$ and $3d_{3/2}$ doublets that are broad and non-symmetrical due to the overlapping of peaks related with the presence of Mo^{4+} at 229.6 eV (50 %), Mo^{5+} at 231.2 eV (48%), and Mo^{6+} species at 232.1 eV (2 %). After the reaction, the MoO_x sample features BEs related to the existence of Mo^{3+} at 228.9 eV (20%), Mo^{4+} at 229.7 eV (30 %), Mo^{5+} at 231.5 eV (17%), and Mo^{6+} species at 232.5 eV (33 %). This assignment of BEs are consistent with the values reported by Choi et al. [73]. The emergence of appreciated amount of new Mo^{3+} species (30%) in the used MoO_x , which is accompanied by a significant diminution of Mo^{4+} species, suggests that the latter underwent an over H_2 -reduction to Mo^{3+} . The population of Mo^{5+} also decreases from 48% to only 14%, while the population of Mo^{6+} increased up to 33%, suggesting also a re-oxidation of Mo^{5+} to Mo^{6+} . Even so, the bulk MoO_x catalyst features a stable catalytic behavior in the GTP reaction, where the propylene yield remains constant at $\sim 59.6\%$ as function of TOS. This suggests that the change in the Mo^{4+} and Mo^{6+} population does not affect the HDO activity; thus, it does not play a significant role in propylene formation. The decrease in the Mo^{5+} population could be recomposing by the emergence of new Mo^{3+} species that seems to be more catalytically active.

In turn, bulk $\beta\text{-Mo}_2\text{C}$, which is pre-carburized and in-situ reduced, features $3d_{5/2}$ and $3d_{3/2}$ signals with a more complex shape due to the overlapped peaks at $\text{Mo}^{2+}\text{-C}$ at 228.3 eV (32%), Mo^{4+} at 229.8 eV (35 %), and Mo^{5+} at 231.3 eV (33 %). The BEs of these peaks are consistent with the assignment of Murugappan et al. for similar Mo carbides. [42] However, these BEs and the percentage of Mo states indicate that the sample was not completely carburized despite the fact that the formation of the carbidic band has been confirmed. The deconvolution of the C1s core-level confirms the presence of the C-Mo band at 282.1 eV and of the adventitious carbon C-C/C=C at 284.8 eV for both fresh and post-reaction $\beta\text{-Mo}_2\text{C}$ samples (Fig. S15 A). Moreover, the used sample features other two peaks at 286.4 eV and 288.8 eV, corresponding to C-O and C=O species, respectively, [74] which are ascribed to carbonaceous species in the form $\text{C}_x\text{H}_y\text{O}_z$. Also, the chemical states and distribution of $\text{Mo}^{\delta+}$ species on the used $\beta\text{-Mo}_2\text{C}$ sample suffered great changes. As a consequence, the 35 % of Mo^{4+} at 229.8 eV completely disappeared, while an equivalent proportion of Mo^{6+} (38 %) appeared at 232.9 eV. However, this surface modification did not affect either the deoxygenation and hydrogenation of glycerol or the yield of propylene, which remain constant at 63.9%, 53.8%, and 49.1%, respectively (Table 5 and Fig. 6). This confirms once more that these Mo^{4+} and Mo^{6+}

states are not catalytically active for the GTP reaction. The slight decrease of the Mo^{5+} species (at 231.7 eV) may be compensated by the formation of the Mo^{3+} state, which cannot be distinguished from the $\text{Mo}^{2+}\text{-C}$ state, appearing at the close BEs (228–229 eV [75]). For this, some increase in the population of $\text{Mo}^{2+}\text{-C}$ was observed, knowing the hydrothermal conditions cannot cause a re-carburization of the sample. The prevalence of the $\text{Mo}^{2+}\text{-C}$ states may be primarily responsible for the glycerol HDO and propylene formation over the carbide and/or oxy-carbide surface.

When $\beta\text{-Mo}_2\text{C}$ was dispersed onto SBA-15, the fresh sample also shows $\text{Mo}^{2+}\text{-C}$ at 228.1 eV (23%), Mo^{4+} at 229.3 eV (34%), and Mo^{5+} at 230.8 eV (43%). The formation of the Mo-C band in this catalyst was also proven by the C1s spectra (Fig. S15 B), which features peaks at 282.1 eV and 284.8 eV, corresponding to C-Mo bands and adventitious carbon, respectively. After the test, the used sample features only BE related to the presence of Mo^{4+} at 229.6 eV (31 %), Mo^{5+} at 230.8 eV (45 %), and Mo^{6+} species at 232.8 eV (25 %). The amount of Mo^{4+} and Mo^{5+} on the used sample is very similar to that of the fresh sample (31–34 % and 43–45 %, respectively). However, the $\text{Mo}^{2+}\text{-C}$ species (23 %) completely disappeared, leading to the emergence of an equivalent proportion of Mo^{6+} (25 %). The absence of the carbide phase after the reaction was proven by the C1s spectrum (Fig. S15 B), which features only bands at 284.8 eV, 286.3 eV, and 288.5 eV, corresponding to adventitious carbon, C-O, and C=O, respectively. The re-oxidation of $\text{Mo}^{2+}\text{-C}$ may have occurred on the highly dispersed Mo carbide particles that are more reactive with the hydrothermal medium or the oxygen of the deposited $\text{C}_x\text{H}_y\text{O}_z$ species. This may be responsible for the decreasing TOF of propylene (from 226.4 h^{-1} to 153.1 h^{-1}) observed for the $\beta\text{-MoC@SBA-15R}$ catalyst (Fig. 7), as we will further corroborate later.

For the fresh $\eta\text{-MoC@SBA-15R}$ catalyst, it features the Mo3d spectra that are relatively similar to those of the $\beta\text{-Mo}_2\text{C@SBA-15R}$ catalyst. Oshikawa et al. [75] also reported that the nature of Mo species revealed by XPS tend to be nearly the same regardless of $\beta\text{-Mo}_2\text{C}$, $\eta\text{-MoC}$, or $\alpha\text{-MoC}_{1-x}$. In fact, the two non-symmetrical shoulders were also deconvoluted into $\text{Mo}^{2+}\text{-C}$ at 228.3 eV (16%), Mo^{4+} at 229.1 eV (50%), and Mo^{5+} at 230.9 eV (34 %). However, the $\eta\text{-MoC@SBA-15R}$ catalyst contains a low amount of $\text{Mo}^{2+}\text{-C}$ and a predominant percentage of Mo^{4+} than of the $\beta\text{-Mo}_2\text{C@SBA-15R}$ catalyst. This agrees with the XRD data (Fig. S7), indicating that the samples carburized under $\text{C}_3\text{H}_6/\text{H}_2$ usually contain the MoO_2 phase. The C1s spectrum (not presented) also indicates the existence of the carbidic C-Mo band at 282.3 eV that completely disappeared in the used $\eta\text{-MoC@SBA-15R}$ sample, suggesting a re-oxidation of $\text{Mo}^{2+}\text{-C}$. Thus, the sum of the $\text{Mo}^{2+}\text{-C}$ and Mo^{5+} proportions (50%) decreased to 43 % for the used $\eta\text{-MoC@SBA-15R}$, while the new Mo^{6+} species (with a significant proportion $\sim 20\%$) reappeared at 232.9 eV. This re-oxidation tendency of partially reduced $\text{Mo}^{\delta+}$ species, particularly Mo^{2+} and Mo^{5+} , may be responsible for the TOF decreasing of the glycerol HDO to propylene (Fig. 7).

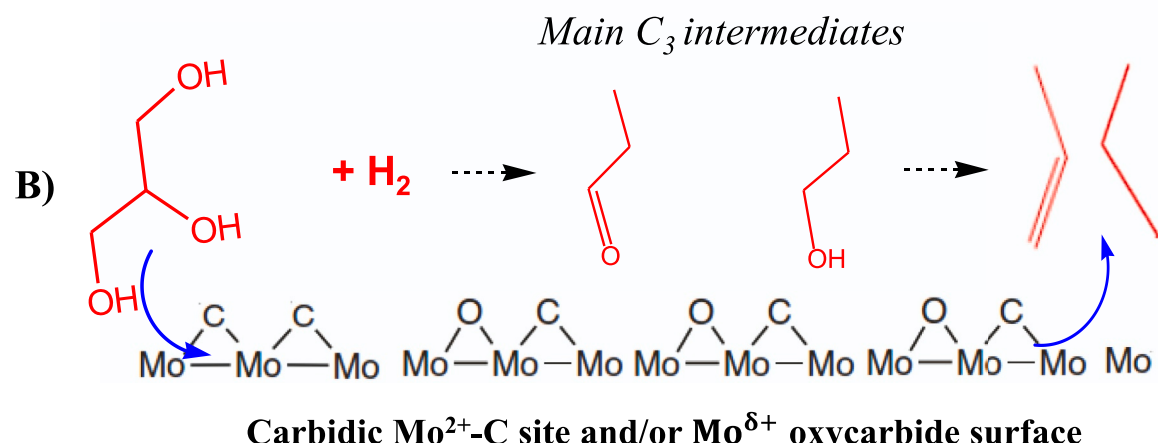
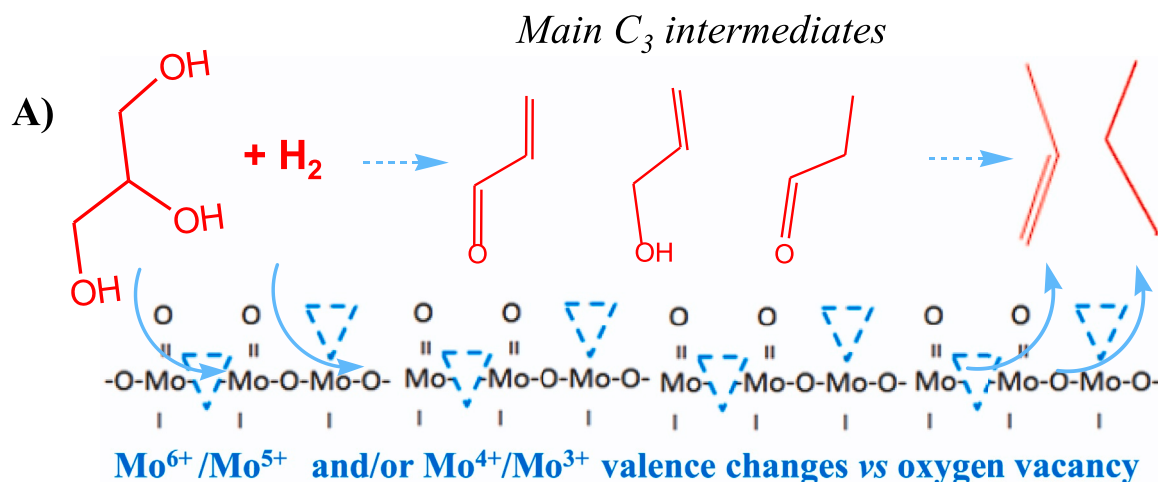
Otherwise, comparing the atomic ratios of C/Mo and O/Mo, we observe that the values are much higher in each used sample compared to its fresh counterpart, which confirms our prior insights, suggesting a deposition of oxygenated carbonaceous species on Mo sites. This also justifies the low intensity of the $3d_{5/2}$ and $3d_{3/2}$ signals in all used samples compared to their fresh counterparts, knowing that sintering of Mo was completely discarded by HRTEM analysis. These carbonaceous species seem to be effectively deposited as $\text{C}_x\text{H}_y\text{O}_z$ rather than a pure graphite. Our observation is in line with those reporting also carbon deposition over Mo_2C during the HDO of acetic acid [64] and anisole [68], but the authors could not put in evidence the accumulation of oxygen on the spent catalyst. Thus, the oxygen accumulation from adsorbed $\text{C}_x\text{H}_y\text{O}_z$ species, which cannot be differentiated to those from H_2O of the medium, appears to be re-oxidizing the Mo species, thereby, leading to loss of HDO activity. Normally, SBA-15 support has hydrophobic characters [46], which could contribute to H_2O repelling. Nevertheless, the dispersed $\beta\text{-Mo}_2\text{C@SBA-15R}$ and $\eta\text{-MoC@SBA-15R}$ catalysts (with an excellent initial deoxygenation activity) accumulate

more oxygen than bulk MoO_x and $\beta\text{-Mo}_2\text{C}$ catalysts. These make us attribute the slight deactivation of Mo based catalyst to oxygen accumulation rather than to carbon itself, contrary to the previous authors [64,68]. Our explanation is supported by i) the emergence of new C-O and C=O bands (at BE of about 286.4 eV and 288.8 eV, respectively) in the C1s core-level of all used samples (see for example Fig. S15 A-B), ii) significant simultaneous increase in the oxygen and carbon content in the surface of the used catalysts, and iii) no significant breaking of the C-C band during the single-step GTP reaction, which is the main precursor of graphitic coke formation. In addition to this, the high amount of oxygen cannot originate from passivation treatment by O_2/He mixture (1/99 vol%) because it is well known that this treatment forms just an atomic oxidized monolayer ($\sim 0.073 \text{ nm}$), while XPS beam usually provide the composition of a minimum interface of $\sim \text{nm}$. In fact, the proportion of passivation oxygen does exceed 1.46% in poor of cases. Thus, the surface accumulation of oxygen from $\text{C}_x\text{H}_y\text{O}_z$ species seem to be a justified cause for $\text{Mo}^{\delta+}$ re-oxidation, and thus, causing slight loss in HDO performance of the dispersed Mo-based systems.

To summarize, we can conclude that the HDO of glycerol to propylene is developed over the MoO_x -based catalyst via successive transition reduction-oxidation cycles of $\text{Mo}^{6+}/\text{Mo}^{5+}$ and $\text{Mo}^{4+}/\text{Mo}^{3+}$ species, as illustrated in Scheme 2 A. The creation of undercoordinated Mo defects, arising from either the H_2 -reduction of MoO_3 to MoO_{3-x} and MoO_2 to MoO_{2-x} , could be acting as an oxygen vacancy susceptible to interactions with the oxygen of glycerol and intermediates. However,

Mo^{6+} and Mo^{4+} states by themselves do not seem to be catalytically active in the single-step GTP route, which updates the early insights of Mota et al.,[22] who reported that the direct reduction of Mo^{6+} to Mo^{4+} is responsible for propylene formation. Zacharopoulou et al.[21] also attributed a positive effect to the presence of Mo^{5+} and, to a lesser extent, Mo^{4+} for propylene formation. Zacharopoulou et al.[21] could not identify Mo^{3+} species as potential active-sites for GTP route. As just revealed by our research, Mo^{4+} species do not directly contribute the to the catalytic act itself.

In contrast, the Mo carbide-based catalysts feature specific $\text{Mo}^{2+}\text{-C}$ species, where their relative population overlapped with those of possible Mo^{3+} formed probably from Mo^{4+} over-reduction, which somehow justifies the improved stability of $\beta\text{-Mo}_2\text{C}$ and the high initial HDO rates of $\beta\text{-Mo}_2\text{C}@\text{SBA-15R}$ and $\eta\text{-MoC}@\text{SBA-15R}$ catalysts. However, after the tests, $\text{Mo}^{2+}\text{-C}$ species completely disappeared on the disposed $\beta\text{-Mo}_2\text{C}@\text{SBA-15R}$ and $\eta\text{-MoC}@\text{SBA-15R}$ catalysts, which was accompanied by an increase in the relative population of Mo^{6+} states, thus leading to a gradual diminution in their GTP yield. This substantial difference in the surface of Mo carbides regarding Mo oxide-based catalysts suggests that most HDO sites in carbides must be different to those of MoO_x -based catalyst. Probably, $\text{Mo}^{2+}\text{-C}$ species are catalytically acting as individual carbide-sites versus oxycarbide sites ($\text{Mo}^{3+}\text{-Mo}^{5+}$ states), as illustrated in Scheme 2 B. Normally, oxycarbide phases are shown to exist on Mo carbides because they are extremely oxophilic species and usually involves an oxygen-rich sub-monolayer when are



Scheme 2. Simplified graphical illustration of the progress of successive deoxygenation and hydrogenation of glycerol and main C_3 intermediates to form propylene over $\text{Mo}^{5+}/\text{Mo}^{6+}$ and/or $\text{Mo}^{3+}/\text{Mo}^{4+}$ redox cycles (A) and $\text{Mo}^{2+}\text{-C}$ carbidic sites or oxycarbide surface (B).

exposed to an oxidant medium [60,64]. Consequently, the mentioned divergence in the surface quality is manifested as a difference in their HDO reactivity and stability. A carbide or oxycarbide surface tends to have more hydrogenator characteristics including at high space-velocity. The relative decrease in the performance of the Mo-based systems seems to be caused by the re-oxidation tendency of $\text{Mo}^{\delta+}$ to form MoO_2 and/or MoO_3 that are more thermodynamically stable than MoO_{2-x} and MoO_{3-x} ones.

Finally, it should be noted that to fully resolve the evolution of the most catalytically active-species for the single-step GTP route, it would be more relevant to combine in-situ ERP and *operando* NAP-XPS analyses with further kinetic measurements. This will allow more precise information about the real-time evolution of the active species as a function of the progress of main deoxygenation and hydrogenation events to be gathered. Even so, our study showed clear responsibility of termed $\text{Mo}^{3+}\text{-O}$, $\text{Mo}^{5+}\text{-O}$, and $\text{Mo}^{2+}\text{-C}$ species in selective HDO of glycerol to propylene. Thus, further studies on the optimal adjustment of the surface oxygen content in highly dispersed Mo oxycarbides and Mo carbide nanoparticles are necessary to develop stable Mo-based catalysts with robust HDO reactivity. The adjustment of chemical states of Mo species can be archived by controlling the initial reduction and carburization and subsequently remodeling the operating conditions, particularly the H_2 -pressure and temperature vis-a-vis the H_2O -partial pressure under which the GTP reaction is taking place.

4. Conclusions

In this work, we provide a systematic structure-properties-performance exploration to further improve the single-step HDO of glycerol to high propylene yield. The strategy consists of modulating the physicochemical properties of Mo-based catalysts for use in an H_2O -rich hydrothermal medium. Thus, we have successfully built and used a novel re-designing approach, providing qualitative and quantitative insights on how to get high loadings of highly reactive sub-2 nm Mo particles onto neutral ordered mesoporous silicas (OMS), which allowed overcome the problematic sintering and leaching of Mo species mainly prominent in H_2O -rich reaction medium. The proposed paradigm offers a good dispersion of MoO_x , $\beta\text{-Mo}_2\text{C}$, and $\eta\text{-MoC}$ species onto OMS, featuring remarkable HDO activities and practically null C-C breaking tendency, which allows the preservation of the high-carbon content along the GTP route.

At a space-velocity of 1.7 h^{-1} , the pre-reduced MoO_x @SBA-15R catalyst (with a low acid/redox site ratio) features a very high propylene yield between 84.1% and 65.6%, while pre-calced MoO_x @SBA-15 C (with a high acid/redox site ratio) mainly yields propionaldehyde (52%). A simple thermal pre-treatment seems to offer a good tool for fine-tuning the selectivity of MoO_x @SBA-15 catalysts towards specific products. However, MoO_x-based MCM-41 or KIT-6 showed the poorest thermal stability despite their good initial GTP performance. At increasing space-velocity (up to 4.5 h^{-1}), the HDO capacity of Mo-O sites tends to be suppressed. However, highly dispersed $\beta\text{-Mo}_2\text{C}$ and $\eta\text{-MoC}$ species maintain good intrinsic HDO activities, providing at steady-state, the highest propylene TOF of 153.1 h^{-1} and 98.2 h^{-1} , respectively, which are at least 3.8 and 2.4 times, respectively, higher than those of bulk $\beta\text{-Mo}_2\text{C}$ and bulk MoO_x systems that have never been reported for state-of-the-art GTP route. Globally, the good geometrical exposure of Mo species improves both C-O removal and C-C hydrogenation without significantly affecting C-C breaking, while the carburization of Mo-O to Mo-C seems to increase these catalytic characteristics and relatively balance the stability. Furthermore, in-situ XPS analyses coupled to kinetic data revealed the existence of partially reduced Mo^{5+} , Mo^{3+} , and $\text{Mo}^{2+}\text{-C}$ species that play an active catalytic role for accomplishing the HDO events in glycerol and intermediates to produce fully deoxygenated and more hydrogenated compounds (i.e., propylene, propane). The whole of these analyses reveals that the single-step GTP route seems to progress; i) over Mo oxide-based catalysts via successive

redox cycles of $\text{Mo}^{5+}/\text{Mo}^{6+}$ and/or $\text{Mo}^{3+}/\text{Mo}^{4+}$ states, and ii) over Mo carbides seems to occur mostly over $\text{Mo}^{2+}\text{-C}$ carbide and oxycarbide surfaces that dispose of more hydrogenator character. The re-oxidation of partially reduced $\text{Mo}^{\delta+}$ states seems to be responsible for the certain loss of HDD activity, which arises from the surface accumulation of oxygen as deposited carbonaceous species. Graphitic coke formation, Mo sintering and/or leaching were completely discarded for these catalysts.

In summary, good control of the Mo physicochemical properties (i.e., particles sizes, chemical states, interaction with inert SBA-15 support, acid/redox sites ratio, etc.) at the synthesis and functionalization steps under a controlled atmosphere (air, hydrogen, or carburizing agent) offers interesting tools to enhance the robustness of HDO catalysts, thus reaching relevant advances in glycerol HDO into propylene. The discussed research approach could be expanded to other types of reactions, particularly those occurring under an aggressive hydrothermal medium. This could drive the development of the next-generation of HDO catalysts and upgrades of many industry-relevant biomass-derived molecules.

CRediT authorship contribution statement

M. El Doukkali: Conceptualization, Methodology, Data curation, Funding acquisition, Investigation, Writing – original draft, Writing – review & editing. **F. Dumeignil:** Resources, Methodology, Funding acquisition, Writing – original draft. **S. Paul:** Resources, Writing - original draft.

Declaration of Competing Interest

The authors declare that they have no known competing financial interests or personal relationships that could have appeared to influence the work reported in this paper.

Data availability

Data will be made available on request.

Acknowledgements

This research is part of CatGTP project, which is an MSCA grant, funded by the EU's H2020 program (agreement No. 101030636). The project leaders thank the FRAPPE program of region "Hauts-de-France" for its support. The REALCAT platform is benefitting from a state subsidy administrated by the French National Research Agency (ANR) within the frame of the 'Future Investments' program (PIA), with the contractual reference 'ANR-11-EQPX-0037'. The European Union, through the ERDF funding administered by the Hauts-de-France Region, has co-financed the platform. Centrale Lille, the CNRS, and University of Lille as well as the Centrale Initiatives Foundation, are thanked for their financial contributions to the acquisition and implementation of the equipment. The authors would also like to thank the technical staff of UCCS's services for their help during the implementation of experiments; high-speed catalytic tests at REALCAT platform (S. Heyte), ICP-OES and CHNS (J. Thuriot-Roukos), in-situ DSC (N. Djellal), in-situ XPS (P. Simon), gas sorption (J. Jezequel, O. Gardoll, and J. Charles), HRTEM-STEM/EDX (M. Marinova) and X-ray diffraction—scattering (L. Burylo and F. Blanchard). The discussions with prof. Royer and Dr. Dhainaut and their help with TGA analysis are gratefully acknowledged.

Appendix A. Supporting information

Supplementary data associated with this article can be found in the online version at doi:10.1016/j.apcatb.2022.122280.

References

- [1] L. Lin, X. Han, B. Han, S. Yang, Emerging heterogeneous catalysts for biomass conversion: studies of the reaction mechanism, *Chem. Soc. Rev.* (2021), <https://doi.org/10.1039/D1CS00039J>.
- [2] P. Sudarsanam, R. Zhong, S.V. den Bosch, S.M. Coman, V.I. Parvulescu, B.F. Sels, Functionalised heterogeneous catalysts for sustainable biomass valorisation, *Chem. Soc. Rev.* vol. 47 (22) (2018) 8349–8402, <https://doi.org/10.1039/C8CS00410B>.
- [3] C. Xu, E. Paone, D. Rodríguez-Padrón, R. Luque, F. Mauriello, Recent catalytic routes for the preparation and the upgrading of biomass derived furfural and 5-hydroxymethylfurfural, *Chem. Soc. Rev.* vol. 49 (13) (2020) 4273–4306, <https://doi.org/10.1039/D0CS00041H>.
- [4] W. Fang, A. Riisager, Recent advances in heterogeneous catalytic transfer hydrogenation/hydrogenolysis for valorization of biomass-derived furanic compounds, *Green Chem.* vol. 23 (2) (2021) 670–688, <https://doi.org/10.1039/D0GC03931D>.
- [5] S. Kim, et al., Recent advances in hydrodeoxygénéation of biomass-derived oxygenates over heterogeneous catalysts, *Green Chem.* vol. 21 (14) (2019) 3715–3743, <https://doi.org/10.1039/C9GC01210A>.
- [6] W. Nabgan, et al., Catalytic biohydrogen production from organic waste materials: a literature review and bibliometric analysis, *Int. J. Hydrog. Energy* vol. 46 (60) (2021) 30903–30925, <https://doi.org/10.1016/j.ijhydene.2021.04.100>.
- [7] W. Liu, et al., Ambient-pressure and low-temperature upgrading of lignin bio-oil to hydrocarbons using a hydrogen buffer catalytic system, *Nat. Energy* vol. 5 (10) (2020) 759–767, <https://doi.org/10.1038/s41560-020-00680-x>.
- [8] C. Hulteberg and J. Brandin, "Process for preparing lower hydrocarbons from glycerol," US20110224470A1, Sep 15, 2011 Accessed: Aug. 25, 2022. [Online]. Available: <https://patents.google.com/patent/US20110224470A1/en>.
- [9] Z.Y. Zakaria, N.A.S. Amin, J. Linnekoski, A perspective on catalytic conversion of glycerol to olefins, *Biomass Bioenergy* vol. 55 (2013) 370–385, <https://doi.org/10.1016/j.biombioe.2013.02.014>.
- [10] G.M. Lari, et al., Environmental and economical perspectives of a glycerol biorefinery, *Energy Environ. Sci.* vol. 11 (5) (2018) 1012–1029, <https://doi.org/10.1039/C7EE03116E>.
- [11] A. Kostyniuk, D. Bajec, B. Likozar, One-step synthesis of ethanol from glycerol in a gas phase packed bed reactor over hierarchical alkali-treated zeolite catalyst materials, *Green Chem.* vol. 22 (3) (2020) 753–765, <https://doi.org/10.1039/C9GC03262B>.
- [12] M. Wang, et al., Catalytic transformation of glycerol to 1-propanol by combining zirconium phosphate and supported Ru catalysts, *RSC Adv.* vol. 6 (35) (2016) 29769–29778, <https://doi.org/10.1039/C6RA02682F>.
- [13] A. Kostyniuk, D. Bajec, P. Djinović, B. Likozar, One-step synthesis of glycitol from glycerol in a gas-phase packed-bed continuous flow reactor over HZSM-5 zeolite catalysts modified by CsNO₃, *Chem. Eng. J.* vol. 394 (2020) 124945, <https://doi.org/10.1016/j.cej.2020.124945>.
- [14] A. Konaka, T. Tago, T. Yoshikawa, A. Nakamura, T. Masuda, Conversion of glycerol into allyl alcohol over potassium-supported zirconia–iron oxide catalyst, *Appl. Catal. B Environ.* vol. 146 (2014) 267–273, <https://doi.org/10.1016/j.apcatb.2013.03.007>.
- [15] A. Kostyniuk, D. Bajec, P. Djinović, B. Likozar, Allyl alcohol production by gas phase conversion reactions of glycerol over bifunctional hierarchical zeolite-supported bi- and tri-metallic catalysts, *Chem. Eng. J.* vol. 397 (2020) 125430, <https://doi.org/10.1016/j.cej.2020.125430>.
- [16] B. Katryniok, S. Paul, M. Capron, F. Dumégnil, Towards the sustainable production of acrolein by glycerol dehydration, *ChemSusChem* vol. 2 (8) (2009) 719–730, <https://doi.org/10.1002/cssc.200900134>.
- [17] M. El Doukkali, et al., A comparison of sol–gel and impregnated Pt or/and Ni based γ -alumina catalysts for bioglycerol aqueous phase reforming, *Appl. Catal. B Environ.* vol. 125 (;&; 2012) 516–529, <https://doi.org/10.1016/j.apcatb.2012.06.024>.
- [18] M. El Doukkali, A. Iriondo, P.L. Arias, J.F. Cambra, I. Gandarias, V.L. Barrio, Bioethanol/glycerol mixture steam reforming over Pt and PtNi supported on lanthana or ceria doped alumina catalysts, *Int. J. Hydrog. Energy* vol. 37 (10) (2012) 8298–8309, <https://doi.org/10.1016/j.ijhydene.2012.02.154>.
- [19] M. El Doukkali, A. Iriondo, I. Gandarias, Enhanced catalytic upgrading of glycerol into high value-added H₂ and propanediols: Recent developments and future perspectives, *Mol. Catal.* vol. 490 (2020), 110928, <https://doi.org/10.1016/j.mcat.2020.110928>.
- [20] E.S. Vasiliadou, A.A. Lemonidou, Glycerol transformation to value added C₃ diols: reaction mechanism, kinetic, and engineering aspects, *WIREs Energy Environ.* vol. 4 (6) (2015) 486–520, <https://doi.org/10.1002/wene.159>.
- [21] V. Zacharopoulou, E.S. Vasiliadou, A.A. Lemonidou, Exploring the reaction pathways of bioglycerol hydrodeoxygénéation to propane over molybdena-based catalysts, *ChemSusChem* vol. 11 (1) (2018) 264–275, <https://doi.org/10.1002/cssc.201701605>.
- [22] C.J.A. Mota, Valter L.C. Gonçalves, J.E. Mellizo, A.M. Rocco, J.C. Fadigas, R. Gambetta, Green propane through the selective hydrogenolysis of glycerol over supported iron-molybdenum catalyst: the original history, *J. Mol. Catal. Chem.* vol. 422 (2016) 158–164, <https://doi.org/10.1016/j.molcata.2015.11.014>.
- [23] M. Monai, M. Gambino, S. Wannakao, B.M. Weckhuysen, Propane to olefins tandem catalysis: a selective route towards light olefins production, *Chem. Soc. Rev.* vol. 50 (20) (2021) 11503–11529, <https://doi.org/10.1039/D1CS00357G>.
- [24] D.S. Lima, O.W. Perez-Lopez, Catalytic conversion of glycerol to olefins over Fe, Mo, and Nb catalysts supported on zeolite ZSM-5, *Renew. Energy* vol. 136 (2019) 828–836, <https://doi.org/10.1016/j.renene.2019.01.051>.
- [25] S.D. Blass, R.J. Hermann, N.E. Persson, A. Bhan, L.D. Schmidt, Conversion of glycerol to light olefins and gasoline precursors, *Appl. Catal. Gen.* vol. 475 (2014) 10–15, <https://doi.org/10.1016/j.apcata.2014.01.013>.
- [26] L. Yu, et al., Propylene from renewable resources: catalytic conversion of glycerol into propylene, *ChemSusChem* vol. 7 (3) (2014) 743–747, <https://doi.org/10.1002/cssc.201301041>.
- [27] Z. Wu, et al., Selective conversion of glycerol into propylene: single-step versus tandem process, *ACS Sustain. Chem. Eng.* vol. 4 (8) (2016) 4192–4207, <https://doi.org/10.1021/acssuschemeng.6b00676>.
- [28] D. Sun, Y. Yamada, S. Sato, Efficient production of propylene in the catalytic conversion of glycerol, *Appl. Catal. B Environ.* vol. 174–175 (2015) 13–20, <https://doi.org/10.1016/j.apcatb.2015.02.022>.
- [29] Z. Wu, et al., MoO₃ modified Ni2P/Al2O₃ as an efficient catalyst for crude glycerol to propylene, *Catal. Commun.* vol. 92 (2017) 80–85, <https://doi.org/10.1016/j.catcom.2017.01.009>.
- [30] A. Chieregato, J.V. Ochoa, F. Cavani, "Olefins from Biomass, in: F. Cavani, S. Albonetti, F. Basile, A. Gandini (Eds.), *Chemicals and Fuels from Bio-Based Building Blocks*, Wiley-VCH Verlag GmbH & Co. KGaA, Weinheim, Germany, 2016, pp. 1–32, <https://doi.org/10.1002/9783527698202.ch1>.
- [31] V. Zacharopoulou, E.S. Vasiliadou, A.A. Lemonidou, One-step propylene formation from bio-glycerol over molybdena-based catalysts, *Green Chem.* vol. 17 (2) (2015) 903–912, <https://doi.org/10.1039/C4GC01307G>.
- [32] F.G. Baddour, C.P. Nash, J.A. Schaidle, D.A. Ruddy, Synthesis of α -MoC_{1–x} nanoparticles with a surface-modified SBA-15 hard template: determination of structure–function relationships in acetic acid deoxygenation, *Angew. Chem. Int. Ed.* vol. 55 (31) (2016) 9026–9029, <https://doi.org/10.1002/anie.201602878>.
- [33] K.-E. You, S.C. Ammal, Z. Lin, W. Wan, J.G. Chen, A. Heyden, Understanding the effect of Mo₂C support on the activity of Cu for the hydrodeoxygénéation of glycerol, *J. Catal.* vol. 388 (2020) 141–153, <https://doi.org/10.1016/j.jcat.2020.05.007>.
- [34] W. Wan, Z. Lin, J.G. Chen, Vibrational spectroscopic characterization of glycerol reaction pathways over metal-modified molybdenum carbide surfaces, *ChemCatChem* vol. 12 (1) (2020) 281–286, <https://doi.org/10.1002/cctc.201901629>.
- [35] G. J, et al., In situ time-resolved X-ray diffraction study of the synthesis of Mo₂C with different carburization agents, *Can. J. Chem.* (2013), <https://doi.org/10.1139/cjc-2012-0516>.
- [36] W.-F. Chen, J.T. Muckerman, E. Fujita, Recent developments in transition metal carbides and nitrides as hydrogen evolution electrocatalysts, *Chem. Commun.* vol. 49 (79) (2013) 8896–8909, <https://doi.org/10.1039/C3CC44076A>.
- [37] Z.Y. Zakaria, J. Linnekoski, N.A.S. Amin, Catalyst screening for conversion of glycerol to light olefins, *Chem. Eng. J.* vol. 207–208 (2012) 803–813, <https://doi.org/10.1016/j.cej.2012.07.072>.
- [38] M. Mellán-Pineiro, N. López, A coupled density functional theory–microkinetic modeling for the hydrodeoxygénéation of glycerol to propylene on MoO₃, *ACS Sustain. Chem. Eng.* vol. 6 (12) (2018) 16169–16178, <https://doi.org/10.1021/acssuschemeng.8b02933>.
- [39] W. Wan, S.C. Ammal, Z. Lin, K.-E. You, A. Heyden, J.G. Chen, Controlling reaction pathways of selective C–O bond cleavage of glycerol, *Nat. Commun.* vol. 9 (1) (2018) 4612, <https://doi.org/10.1038/s41467-018-07047-7>.
- [40] Y. Wang, et al., Towards rational catalyst design: boosting the rapid prediction of transition-metal activity by improved scaling relations, *Phys. Chem. Chem. Phys.* vol. 21 (35) (2019) 19269–19280, <https://doi.org/10.1039/C9CP04286E>.
- [41] F. Calle-Vallejo, D. Loffreda, M.T.M. Koper, P. Sautet, Introducing structural sensitivity into adsorption–energy scaling relations by means of coordination numbers, *Nat. Chem.* vol. 7 (5) (2015) 403–410, <https://doi.org/10.1038/nchem.2226>.
- [42] K. Murugappan, E.M. Anderson, D. Teschner, T.E. Jones, K. Skorupska, Y. Román-Leshkov, Operando NAP-XPS unveils differences in MoO₃ and Mo₂C during hydrodeoxygénéation, *Nat. Catal.* vol. 1 (12) (2018) 960–967, <https://doi.org/10.1038/s41929-018-0171-9>.
- [43] G. Zichitella, Y. Polychák, R. Tschaggelar, G. Jeschke, J. Pérez-Ramírez, Quantification of redox sites during catalytic propane oxychlorination by operando EPR spectroscopy, *Angew. Chem. Int. Ed.* vol. 60 (7) (2021) 3596–3602, <https://doi.org/10.1002/anie.202013331>.
- [44] A. Borowiec, et al., An acrolein production route from ethanol and methanol mixtures over FeMo-based catalysts, *Green Chem.* vol. 19 (11) (2017) 2666–2674, <https://doi.org/10.1039/C7GC00341B>.
- [45] S. Chen, et al., Preparation of nickel (oxide) nanoparticles confined in the secondary pore network of mesoporous scaffolds using melt infiltration, *Catal. Today* vol. 334 (9) (2019) 48–58, <https://doi.org/10.1016/j.cattod.2019.01.064>.
- [46] D.P. Serrano, G. Calleja, J.A. Botas, F.J. Gutierrez, Adsorption and hydrophobic properties of mesostructured MCM-41 and SBA-15 materials for volatile organic compound removal, *Ind. Eng. Chem. Res.* vol. 43 (22) (2004) 7010–7018, <https://doi.org/10.1021/ie040108d>.
- [47] X.-H. Wang, H.-L. Hao, M.-H. Zhang, W. Li, K.-Y. Tao, Synthesis and characterization of molybdenum carbides using propane as carbon source, *J. Solid State Chem.* vol. 179 (2) (2006) 538–543, <https://doi.org/10.1016/j.jssc.2005.11.009>.
- [48] D. Zhao, et al., Triblock copolymer syntheses of mesoporous silica with periodic 50 to 300 angstrom pores, *Science* vol. 279 (5350) (1998) 548–552, <https://doi.org/10.1126/science.279.5350.548>.
- [49] C.T. Kresge, M.E. Leonowicz, W.J. Roth, J.C. Vartuli, J.S. Beck, Ordered mesoporous molecular sieves synthesized by a liquid-crystal template mechanism, *Nature* vol. 359 (6397) (1992) 710–712, <https://doi.org/10.1038/359710a0>.

- [50] F. Kleitz, S.H. Choi, R. Ryoo, Cubic Ia3d large mesoporous silica: synthesis and replication to platinum nanowires, carbon nanorods and carbon nanotubes, *Chem. Commun.* no. 17 (2003) 2136–2137, <https://doi.org/10.1039/B306504A>.
- [51] A. Travert, et al., Parallel between infrared characterisation and ab initio calculations of CO adsorption on sulphided Mo catalysts, *Catal. Today* vol. 70 (1) (2001) 255–269, [https://doi.org/10.1016/S0920-5861\(01\)00422-9](https://doi.org/10.1016/S0920-5861(01)00422-9).
- [52] J. Raskó, J. Kiss, Infrared study of the adsorption of CO and CH₃ on silica-supported MoO₃ and Mo₂C catalysts, *Appl. Catal. Gen.* vol. 253 (2) (2003) 427–436, [https://doi.org/10.1016/S0926-860X\(03\)00555-6](https://doi.org/10.1016/S0926-860X(03)00555-6).
- [53] W. Wu, Z. Wu, C. Liang, X. Chen, P. Ying, C. Li, In Situ FT-IR spectroscopic studies of CO adsorption on fresh Mo₂C/Al₂O₃ catalyst, *J. Phys. Chem. B* vol. 107 (29) (2003) 7088–7094, <https://doi.org/10.1021/jp027582m>.
- [54] T.M. Eggenhuisen, J.P. den Breejen, D. Verdoes, P.E. de Jongh, K.P. de Jong, Fundamentals of melt infiltration for the preparation of supported metal catalysts. The case of Co/SiO₂ for Fischer–Tropsch synthesis, *J. Am. Chem. Soc.* vol. 132 (51) (2010) 18318–18325, <https://doi.org/10.1021/ja1080508>.
- [55] S.K. Jana, A. Mochizuki, S. Namba, Progress in pore-size control of mesoporous MCM-41 molecular sieve using surfactant having different alkyl chain lengths and various organic auxiliary chemicals, *Catal. Surv. Asia* vol. 8 (1) (2004) 1–13, <https://doi.org/10.1023/B:CATS.0000015110.85694.d9>.
- [56] S. Paul, S. Heyte, B. Katryniok, C. García-Sancho, P. Maireles-Torres, F. Dumeignil, REALCAT: a new platform to bring catalysis to the lightspeed, *Oil Gas. Sci. Technol. – Rev. D'IFP Energ. Nouv.* vol. 70 (3) (2015) 455–462, <https://doi.org/10.2516/ogst/2014052>.
- [57] R.L. Brutchev, D.A. Ruddy, L.K. Andersen, T.D. Tilley, Influence of surface modification of Ti–SBA15 catalysts on the epoxidation mechanism for cyclohexene with aqueous hydrogen peroxide, *Langmuir* vol. 21 (21) (2005) 9576–9583, <https://doi.org/10.1021/la051182j>.
- [58] M.L. Shozai, V.D.B.C. Dasireddy, S. Singh, P. Mohlala, D.J. Morgan, H.B. Friedrich, Hydrogenolysis of Glycerol to monoalcohols over supported Mo and W catalysts, *ACS Sustain. Chem. Eng.* vol. 4 (10) (2016) 5752–5760, <https://doi.org/10.1021/acssuschemeng.6b01675>.
- [59] V.O.O. Gonçalves, et al., Effect of the support on the hydrodeoxygenation of m-cresol over molybdenum oxide based catalysts, *Appl. Catal. B Environ.* vol. 214 (2017) 57–66, <https://doi.org/10.1016/j.apcatb.2017.05.003>.
- [60] T. Prasomrsl, T. Nimmanwudipong, Y. Román-Leshkov, Effective hydrodeoxygenation of biomass-derived oxygenates into unsaturated hydrocarbons by MoO₃ using low H₂ pressures, *Energy Environ. Sci.* vol. 6 (6) (2013) 1732–1738, <https://doi.org/10.1039/C3EE24360E>.
- [61] P. Delporte, F. Meunier, C. Pham-Huu, P. Vennegues, M.J. Ledoux, J. Guille, Physical characterization of molybdenum oxycarbide catalyst; TEM, XRD and XPS, *Catal. Today* vol. 23 (3) (1995) 251–267, [https://doi.org/10.1016/0920-5861\(94\)00166-Y](https://doi.org/10.1016/0920-5861(94)00166-Y).
- [62] D.R. Stellwagen, J.H. Bitter, Structure–performance relations of molybdenum- and tungsten carbide catalysts for deoxygenation, *Green Chem.* vol. 17 (1) (2014) 582–593, <https://doi.org/10.1039/C4GC01831A>.
- [63] T. Mo, J. Xu, Y. Yang, Y. Li, Effect of carburization protocols on molybdenum carbide synthesis and study on its performance in CO hydrogenation, *Catal. Today* vol. 261 (2016) 101–115, <https://doi.org/10.1016/j.cattod.2015.07.014>.
- [64] J.A. Schaidle, et al., Experimental and computational investigation of acetic acid deoxygenation over oxophilic molybdenum carbide: surface chemistry and active site identity, *ACS Catal.* vol. 6 (2) (2016) 1181–1197, <https://doi.org/10.1021/acscatal.5b01930>.
- [65] X. Gao, et al., State-of-art modifications of heterogeneous catalysts for CO₂ methanation – Active sites, surface basicity and oxygen defects, *Catal. Today* (2022), <https://doi.org/10.1016/j.cattod.2022.03.017>.
- [66] C. Ciotoanea, et al., Improved dispersion of transition metals in mesoporous materials through a polymer-assisted melt infiltration method, *Catal. Sci. Technol.* vol. 7 (22) (2017) 5448–5456, <https://doi.org/10.1039/C7CY00963A>.
- [67] Z.-K. Liu, J. Ågren, M. Hillert, Application of the Le Chatelier principle on gas reactions, *Fluid Phase Equilibria* vol. 121 (1) (1996) 167–177, [https://doi.org/10.1016/0378-3812\(96\)02994-9](https://doi.org/10.1016/0378-3812(96)02994-9).
- [68] W.-S. Lee, A. Kumar, Z. Wang, A. Bhan, Chemical titration and transient kinetic studies of site requirements in Mo₂C-catalyzed vapor phase anisole hydrodeoxygenation, *ACS Catal.* vol. 5 (7) (2015) 4104–4114, <https://doi.org/10.1021/acscatal.5b00713>.
- [69] Y. Liu, et al., From glycerol to allyl alcohol: iron oxide catalyzed dehydration and consecutive hydrogen transfer, *Chem. Commun.* vol. 46 (8) (2010) 1238–1240, <https://doi.org/10.1039/B921648K>.
- [70] A.D. Anderson, M.P. Lanci, J.S. Buchanan, J.A. Dumesic, G.W. Huber, The hydrodeoxygenation of glycerol over NiMoSx: Catalyst stability and activity at hydropyrolysis conditions, *ChemCatChem* vol. 13 (1) (2021) 425–437, <https://doi.org/10.1002/cctc.202001289>.
- [71] V. Zacharopoulou, A.A. Lemonidou, Novel process for propene production from biomass: catalytic glycerol hydro-deoxygenation, *Mater. Today Proc.* vol. 5 (14) (2018) 27511–27516, <https://doi.org/10.1016/j.matpr.2018.09.070>.
- [72] E.S. Vasiliadou, A.A. Lemonidou, Kinetic study of liquid-phase glycerol hydrogenolysis over Cu/SiO₂ catalyst, *Chem. Eng. J.* vol. 231 (2013) 103–112, <https://doi.org/10.1016/j.cej.2013.06.096>.
- [73] J.-G. Choi, L.T. Thompson, XPS study of as-prepared and reduced molybdenum oxides, *Appl. Surf. Sci.* vol. 93 (2) (1996) 143–149, [https://doi.org/10.1016/0169-4332\(95\)00317-7](https://doi.org/10.1016/0169-4332(95)00317-7).
- [74] D. Wang, J. Wang, X. Luo, Z. Wu, L. Ye, In situ preparation of Mo₂C nanoparticles embedded in ketjenblack carbon as highly efficient electrocatalysts for hydrogen evolution, *ACS Sustain. Chem. Eng.* vol. 6 (1) (2018) 983–990, <https://doi.org/10.1021/acssuschemeng.7b03317>.
- [75] K. Oshikawa, M. Nagai, S. Ormi, Characterization of molybdenum carbides for methane reforming by TPR, XRD, and XPS, *J. Phys. Chem. B* vol. 105 (38) (2001) 9124–9131, <https://doi.org/10.1021/jp0111867>.